Nano Research

Open Access

Review Article

Laser processing technologies for solar-driven interfacial evaporation

Zhihao Yang[1,2], Zihao Song[2], Yifei Zhao[2], Jinhao Zhang[1,2], Bin Wang[2], Fei Zhao[1], Yang Zhao[1], Huhu Cheng[2] ✉, Lan Jiang[3], and Liangti Qu[2] ✉

[1] *Key Laboratory of Cluster Science, Ministry of Education of China, Beijing Key Laboratory of Photoelectronic/Electrophotonic Conversion Materials, School of Chemistry and Chemical Engineering, Beijing Institute of Technology, Beijing 100081, China*
[2] *Key Laboratory of Organic Optoelectronics & Molecular Engineering, Ministry of Education, State Key Laboratory of Flexible Electronics Technology, Department of Chemistry, Tsinghua University, Beijing 100084, China*
[3] *Laser Micro/Nano-Fabrication Laboratory, School of Mechanical Engineering, Beijing Institute of Technology, Beijing 100081, China*

Cite this article: *Nano Research*, **2026**, *19*, 94908393. https://doi.org/10.26599/NR.2026.94908393

ABSTRACT: The global scarcity of water resources poses substantial challenges to human society, prompting the need for innovative solutions. Recently developed solar-driven interfacial evaporation (SDIE) has emerged as an effective approach to harvest clean water with low cost and eco-friendliness. Laser processing technology, characterized by its simplicity, efficiency, and sustainability, has attracted significant interest within the domain of SDIE. In this review, the conversion of solar energy into thermal energy and the mechanisms of water transport for SDIE are first introduced. Then, laser etching, laser-induced graphitization (LIG), laser *in-situ* synthesis of LIG/composites, liquid-phase pulsed evaporation, and so on, laser processing techniques for modifying material properties to enhance water evaporation performance are discussed, as well as the advantages and limitations. Finally, the review offers a forward-looking perspective on potential future advancements, which would provide the insight into the domain of laser processing technologies for SDIE.

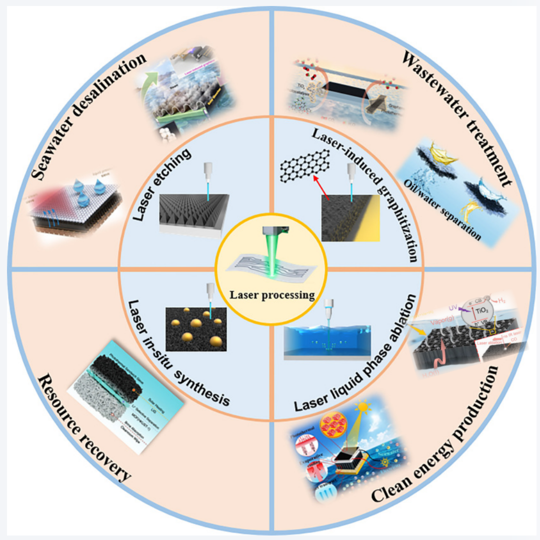

KEYWORDS: solar-driven interfacial evaporation, laser processing technology, laser-induced graphitization, laser etching

1 Introduction

The ongoing increase in the global population, coupled with the rapid pace of industrialization, has rendered water scarcity a significant constraint on the sustainable development of human society [1]. Within this context, the development of efficient and sustainable water treatment technologies, coupled with the adoption of clean energy utilization strategies, is critically important. Harnessing abundant solar energy to produce clean water represents a green and sustainable approach [2]. Conventional solar water evaporation methods generally rely on heating the base of the bulk water [3] or applying bulk heating [4], leading to low efficiency in solar-to-steam energy conversion. Conversely, solar-driven interfacial evaporation (SDIE) technology effectively localizes solar energy at the gas–liquid interface [5], thereby promoting rapid steam generation and significantly improving the efficiency of solar-to-steam energy conversion [6]. The main factors affecting the performance of SDIE are the efficiency with which solar energy is converted into thermal energy and the mass transport properties of the bulk water to the evaporation interface [7–9]. Numerous studies have focused on improving and optimizing solar evaporators based on these two factors [10–12], and many investigations have employed laser processing technology to accomplish this objective [13, 14].

Laser processing technology, recognized as an advanced material processing method, has been extensively utilized across various domains, including electrochemical energy storage [15, 16], flexible electronics [16–18], chemical sensors [19], and photoelectric detection [20], this widespread application is attributed to its unique benefits, such as high precision, operational efficiency, and non-contact processing capabilities. Laser processing enables the rapid

Received: December 9, 2025; **Revised:** December 29, 2025
Accepted: December 30, 2025

✉Address correspondence to Huhu Cheng, huhucheng@tsinghua.edu.cn; Liangti Qu, lqu@mail.tsinghua.edu.cn

and eco-friendly synthesis of photothermal materials, such as metal nanoparticles [21], semiconductor materials [22, 23], and carbon-based materials [24]. Additionally, it allows for the precise fabrication of micro-nanostructures on material surfaces. These advancements contribute to enhanced solar absorption and increased photothermal conversion efficiency, thereby garnering considerable interest within the domain of photothermal interfacial evaporation. Furthermore, laser processing technology facilitates the fabrication of specialized structures [25] and composite materials [26], thereby enabling multifunctional synergistic optimization through photothermal interfacial evaporation. This characteristic has endowed this technology with significant potential for development in this field.

This review article offers a comprehensive overview of recent advancements in laser processing technologies applied to SDIE. It commences with an examination of the key factors influencing SDIE performance. Subsequently, a detailed analysis was conducted on four laser processing techniques—laser etching, laser-induced graphitization (LIG), laser *in-situ* synthesis of LIG/composites, and liquid-phase pulsed evaporation—along with their respective applications in solar interfacial evaporation (Fig. 1). The discussion highlights the specific functionalities of each method and their distinct advantages in the fabrication of interfacial evaporation materials. Finally, the challenges associated with the application of laser processing technology in the SDIE domain were analyzed, and potential future development directions were explored. The aim of this review is to furnish researchers in the field with valuable references and insights to facilitate the continued advancement of solar interfacial evaporation technologies.

2 Key performance characteristics of SDIE materials

2.1 Photothermal conversion

Solar radiation comprises electromagnetic waves made up of photons exhibiting a range of frequencies. The material can absorb the energy carried by these photons, thereby triggering various

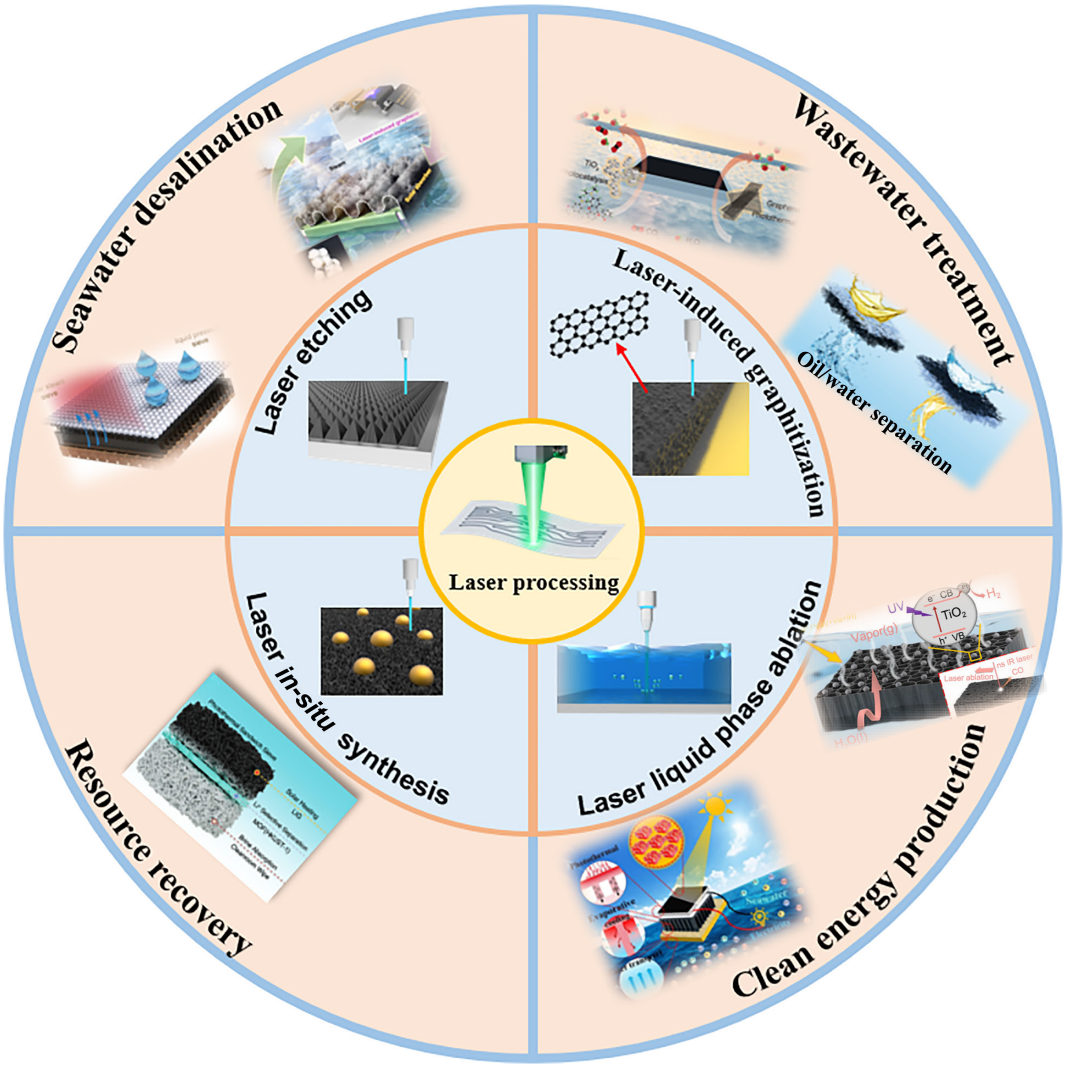

Figure 1 The application of laser processing in the SDIE [27], including seawater desalination [28, 29], wastewater treatment [30, 31], clean energy production [32, 33], and resource recovery [34]. Reproduced with permission from Ref. [27], © Wiley-VCH GmbH 2023. Reproduced with permission from Ref. [28], © Zhang, S. et al. 2023. Reproduced with permission from Ref. [29], © American Chemical Society 2024. Reproduced with permission from Ref. [30], © Elsevier B.V. 2025. Reproduced with permission from Ref. [31], © American Chemical Society 2024. Reproduced with permission from Ref. [32], © American Chemical Society 2025. Reproduced with permission from Ref. [33], © Elsevier B.V. 2025. Reproduced with permission from Ref. [34], © Wiley-VCH GmbH 2024.

energy conversion processes. Among them, the photothermal effect is one of the most common phenomena. The efficiency of photothermal conversion is a crucial determinant affecting SDIE. Laser processing technology has been demonstrated to significantly improve the photothermal conversion capabilities of materials, which underpins its widespread application in the domain of photothermal interfacial evaporation. The mechanisms responsible for photothermal conversion differ according to the specific material involved; the following sections will outline three separate pathways of conversion.

2.1.1 Plasmon resonance effect

The surface plasmon resonance phenomenon pertains to the coherent oscillation of electrons induced when the frequency of incident photons corresponds to the intrinsic frequency of electrons at the surface [36]. This phenomenon typically takes place in metallic materials with a high density of free electrons at the surface. When plasmonic nanometals are excited by photons, the oscillation of free electrons generates high-energy hot carriers through non-radiative energy dissipation pathways, also known as Landau damping processes [37]. The energy carried by these hot carriers is subsequently converted into thermal energy through interactions with phonon modes, thereby enabling photothermal conversion (Fig. 2(a)). Laser processing of metal substrates can enhance the plasmonic effect. By using laser etching technology, microstructures can be fabricated on the metal surface, confining the light within the microstructures and significantly increasing the solar absorption rate, thereby enhancing the photothermal conversion.

2.1.2 Non-radiative relaxation

Photothermal conversion in semiconductor materials predominantly occurs through the non-radiative relaxation processes of electron–hole pairs. When the energy of incident photons meets or exceeds the bandgap energy, the semiconductor absorbs these photons, resulting in the excitation of electrons from the valence band to the conduction band and the concurrent generation of holes within the valence band. The energy possessed by the excited electrons is dissipated via non-radiative relaxation mechanisms; in particular, the high-energy excited electrons often undergo collisions with phonons, thereby transferring their energy to the lattice [38]. This process enhances lattice vibrations, leading to an elevation in the surface temperature of the material (Fig. 2(b)). Through the deliberate design of the semiconductor's structural and compositional attributes, its band structure can be modulated, enabling the adjustment of its solar absorption properties [39]. Laser processing technology facilitates not only the fabrication of semiconductor materials but also the modulation of the semiconductor band gap. Additionally, it can also load metal nanoparticles onto the surface of semiconductors to harness plasmonic effects, thereby improving the photothermal conversion efficiency of the semiconductor materials.

2.1.3 Molecular thermal vibrations

In contrast to non-radiative relaxation processes, molecular thermal vibrations within conjugated materials promote photothermal conversion. Specifically, when the energy of incident photons corresponds to the electronic transition energy, the conjugated π electrons undergo excitation from the highest occupied molecular orbital (HOMO) to the lowest unoccupied molecular orbital (LUMO). The excited electrons then relax back to the ground state through electron–phonon coupling, transferring energy that drives lattice vibrations and causes the material's temperature to rise (Fig. 2(c)) [40]. The conjugation or hyperconjugation of π orbitals plays a critical role in modulating the electronic transitions between the HOMO and the LUMO. In carbon-based materials or conjugated polymers characterized by extensive networks of sp^2-hybridized carbon atoms, the energy gap between the HOMO and the LUMO decreases as the number of π bonds increases [10].

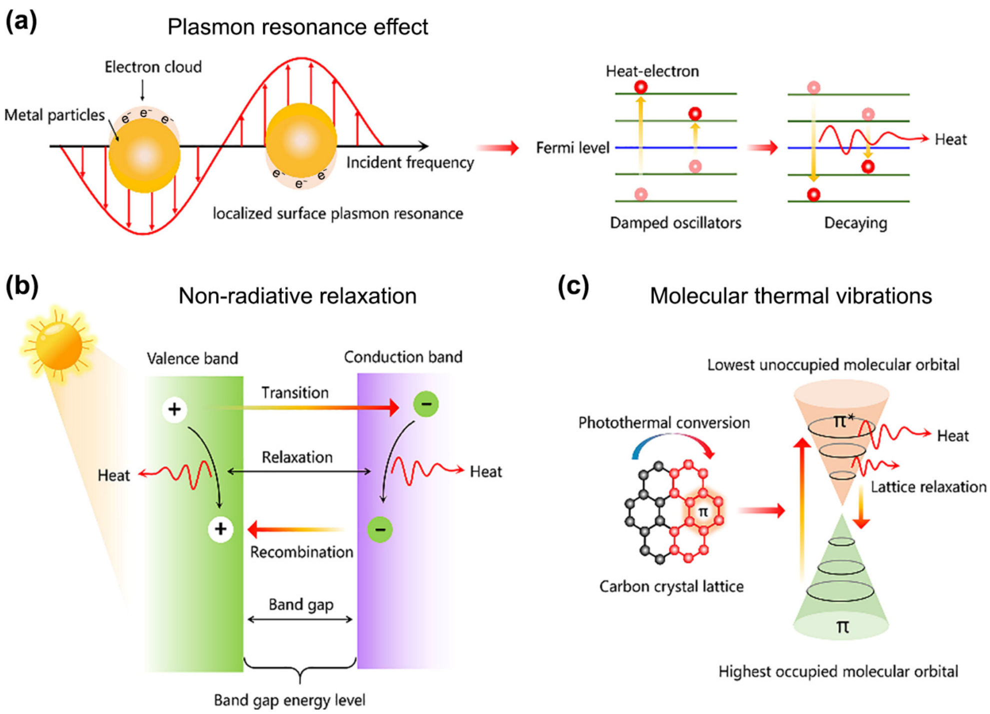

Figure 2 Schematic diagram of the photothermal conversion mechanism: (a) plasmon resonance effect, (b) non-radiative relaxation, and (c) molecular thermal vibration. Reproduced with permission from Ref. [35], © Elsevier Inc. 2024.

Common conjugated materials include carbon nanomaterials, such as carbon nanotubes [41], graphene [42], and graphene oxide (GO) [43–45], which contain a high density of sp^2-hybridized carbon atoms and are rich in delocalized π electrons. These π electrons have low binding energy, allowing electronic transitions to be excited by light across a broad wavelength range, thereby enabling full absorption of sunlight. This property makes them excellent candidates for solar-driven photothermal water evaporation materials [40, 46]. Additionally, some conjugated polymers, such as polyaniline (PAN) [47] and polypyrrole (PPY) [48–50], possess continuous π-conjugated carbon backbones and are among the material systems capable of achieving efficient solar photothermal water evaporation [51].

2.2 Surface wettability

Beyond attaining efficient solar-to-thermal energy conversion, surface wettability plays a critical role [52, 53]. It not only affects the water transport mechanisms but also exerts a substantial influence on the evaporation rate [11]. The heat transfer efficiency during the evaporation process is contingent upon the dynamic behavior of the liquid film, which is governed by the wettability and morphological characteristics of the solid surface [54]. Wettability influences the morphology of liquid droplets on solid substrates and is commonly quantified by the contact angle [55, 56].

On a smooth, chemically homogeneous surface, a droplet will maintain a stable state (Fig. 3(a)). The intrinsic contact angle (θ_Y) is related to the three surface tensions at the contact line by Young's equation [58]

$$\gamma_{sv} = \gamma_{sl} + \gamma_{lv}\cos\theta_Y \tag{1}$$

The γ_{sv}, γ_{sl}, and γ_{lv} represent the surface tensions of the solid–vapor, solid–liquid, and liquid–vapor interfaces, respectively. In reality, solid surfaces are typically rough, which leads to varied liquid wetting behaviors. In 1936, Wenzel was the first to provide a theoretical explanation for the influence of surface roughness on the contact angle [59], positing that surface roughness enhances the wetting properties of a liquid on a solid substrate. When a droplet is in intimate contact with a rough surface (Fig. 3(b)), the material demonstrates hydrophilic behavior, consistent with the Wenzel state model. In this model, the apparent contact angle, denoted as θ_W, is characterized by Eq. (2)

$$\cos\theta_W = r\cos\theta_Y \tag{2}$$

where r denotes the roughness factor, defined as the ratio between the actual solid surface area and its projected area. The equation demonstrates that surface roughness (where $r > 1$) enhances the wetting characteristics. Utilizing the Wenzel state model to predict surface wettability suggests that surface roughness intensifies the intrinsic wettability properties of a surface, thereby augmenting hydrophilicity in hydrophilic surfaces and reinforcing hydrophobicity in hydrophobic surfaces. Nevertheless, this model is limited in its applicability and does not hold when the rough features of the solid surface are not completely wetted by water. In 1944, Cassie and Baxter proposed an alternative solid–liquid contact configuration [60], wherein the droplet is supported by the microstructures present on the solid surface (Fig. 3(c)). This configuration is referred to as the Cassie–Baxter state. The apparent contact angle, denoted as θ_C, in this state is described by Eq. (3)

$$\cos\theta_C = f\cos\theta_Y - 1 + f \tag{3}$$

The f represents the fraction of the solid–liquid interface beneath the droplet. In the Cassie–Baxter state, the droplet is suspended on the microscopic structures of the solid, interacting only partially with the tips of these structures and forming a gas "cushion" beneath the droplet [61]. This structure reduces the solid–liquid contact area, resulting in a high contact angle and imparting hydrophobic characteristics to the material [62]. According to the Cassie–Baxter model, micro-nano structures on surfaces can enhance their inherent wettability, rendering hydrophilic surfaces more hydrophilic and hydrophobic surfaces more hydrophobic. Laser processing enables the precise fabrication of micro- and nanostructures on material surfaces. By appropriately selecting the substrate and optimizing the corresponding laser processing parameters, it is possible to produce superhydrophilic or superhydrophobic surfaces.

2.3 Capillary effect

Although the surface wettability of the material contributes to water transport, wettability alone is insufficient to satisfy the water supply demands of high-speed interfacial evaporation. An optimal water transmission effect can be achieved solely through the integration of capillary effect [63]. In 1921, Edward W. Washburn conducted a systematic investigation into the dynamics of liquid flow within capillaries and porous materials [64]. By positing that, driven by capillary forces, the liquid ascends along a V-shaped groove (Fig. 3(d)), the phenomenon can be mathematically characterized by Eq. (4) [65]

$$Z^2 = K(\alpha,\theta)\frac{\gamma h_0}{\mu}t \tag{4}$$

where Z represents the liquid level height in the capillary. $K(\alpha, \theta)$ is a geometric parameter influenced by the groove angle α and the solid–liquid interface contact angle (θ). γ denotes the liquid surface tension, h_0 is the groove height, μ is the liquid viscosity, and t represents the time it takes for the liquid to diffuse within the capillary tube. According to this model, the height of the liquid level is strongly correlated with the contact angle at the solid–liquid interface and exhibits a proportional relationship with $\cos\theta$ [66].

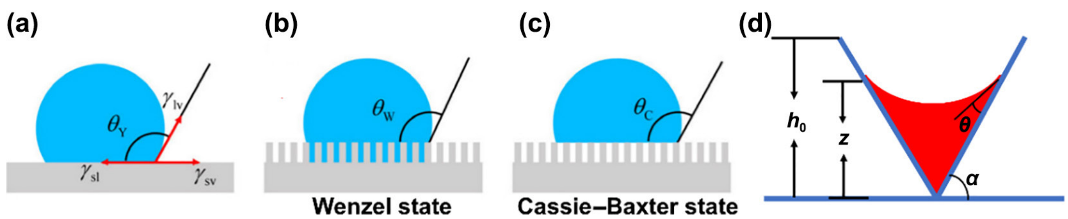

Figure 3 Schematic diagrams of different wetting states and capillary effects of droplets residing on solid surfaces. (a) A static droplet on a smooth surface with an intrinsic contact angle. Static droplets on structured surfaces in the (b) Wenzel state and (c) Cassie–Baxter state. Reproduced with permission from Ref. [57], © Liu, X. et al. 2025. (d) Schematic diagram of capillary effects.

The micro-nanostructures of the material surface not only improve its hydrophilicity but also augment the capillary effect. The combined influence of these factors facilitates the continuous transport of bulk water to the evaporation interface, thereby establishing a robust basis for efficient photothermal water evaporation [67].

3 Application of laser etching process in SDIE

Laser etching is among the most widely utilized laser processing techniques [68]. In this process, a high-energy pulsed laser beam is focused onto the material surface following a predetermined path, resulting in selective ablation and the formation of micro-nanoscale structures on the material surface [69] (Fig. 4(a)). By precisely adjusting laser processing parameters, including laser wavelength, pulse frequency, and scan line width, it is possible to fabricate micro-structures with diverse morphologies [25]. The subsequent section offers a summary of recent research developments in using laser etching in SDIE.

Microstructures fabricated on metal surfaces serve to confine incident light within these features, thereby reducing outward reflection and enhancing absorption [70] (Fig. 5(a)). When integrated with plasmonic phenomena, this method can significantly enhance the photothermal conversion efficiency of the material. The fabricated microstructures exhibit a diverse range of morphologies. For example, a micro-hill structure adorned with nano-scale snowflake-like features was engineered on the surface of Al foil [71], resulting in a substantial increase in solar absorption efficiency. Additionally, the surface appearance transformed from silver to black (see Fig. 5(b)). Alternatively, the structure may consist of micro-pyramids (Fig. 5(c)), which exhibit superior solar absorption capabilities (96% absorption rate, Fig. 5(d)). Additionally, this configuration demonstrates exceptional photothermal conversion efficiency, reaching temperatures up to 83.8 °C under standard solar irradiation (Fig. 5(e)) [72]. Importantly, this design maintains effective solar absorption across a broad spectrum of incident angles, thereby making it suitable for application in diverse geographic regions worldwide. The laser etching technique is compatible with both metallic and carbon-based materials [74]. A fish-scale-inspired pattern can be engineered on the surface of the GO-sodium alginate (SA) composite hydrogel (GAH) (Fig. 5(f)), attaining 95% absorption under full-spectrum sunlight, which markedly surpasses that of a non-biomimetic reduced GO (rGO)/alginate hydrogel (Figs. 5(g) and 5(h)). This design resulted in a high evaporation rate of 2.51 $kg\cdot m^{-2}\cdot h^{-1}$ [73].

Micro-nanostructures not only induce a light-trapping effect but also increase surface roughness, thereby enhancing hydrophilicity and achieving superwetting of water on the material surface [75] (Fig. 6(a)). In conjunction with capillary effects, these features facilitate continuous water pumping to the evaporation interface, promoting water evaporation. The fabrication of ordered micro-groove arrays on the surface of Al foil significantly enhances hydrophilicity and capillary effect of the surface [66]. It can be clearly observed that, driven by capillary action, water is transported upward against the force of gravity (Fig. 6(b)). These observations corresponded with predictions from the classical Washburn model (Fig. 6(c)). Based on this, the researchers designed a more complex and orderly "micro-steam volcano structures" on copper foil using both nanosecond and femtosecond lasers (Fig. 6(d)). The larger grooves located at the edges of the micro-cones functioned as primary water transport channels (Fig. 6(d)(I)), enabling rapid and long-distance liquid transport. Narrower micro-grooves situated between the micro-cone arrays served as secondary water pumping channels, directing liquid flow from the grooves toward the periphery of the micro-cones (Fig. 6(d)(II)). Additionally, submicron ripples and abundant nanoparticles on the micro-cone surfaces further facilitated upward liquid pumping (Fig. 6(d)(III)), ultimately forming an extended thin liquid film that fully covered the micro-cones. Owing to the precise design and arrangement of the triple-level super-wicking evaporation surface (TWES) capillary pathways, the instantaneous water transport velocity within the micro-cone structures reached 88 $mm\cdot s^{-1}$, resulting in a high evaporation rate of 3.33 $kg\cdot m^{-2}\cdot h^{-1}$ [76].

In conventional evaporators, water transport and evaporation occur on the same plane, resulting in the generated water vapor diminishing the solar energy absorption at the evaporation

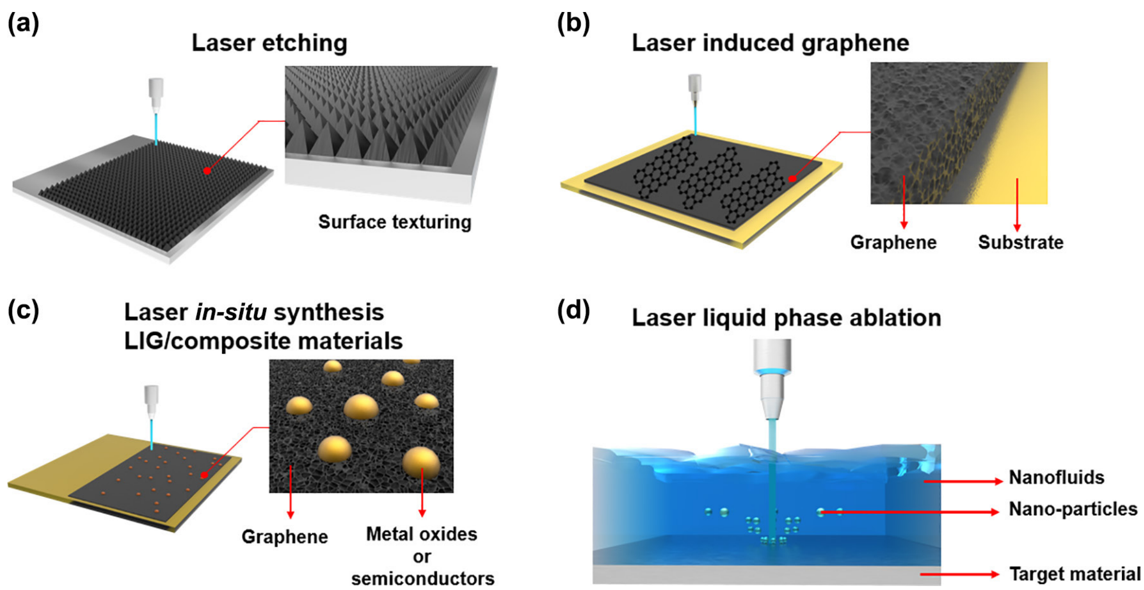

Figure 4 Schematic diagram of laser processing technologies: (a) laser etching, (b) LIG, (c) laser *in-situ* synthesis LIG/composite materials, and (d) laser liquid-phase ablation.

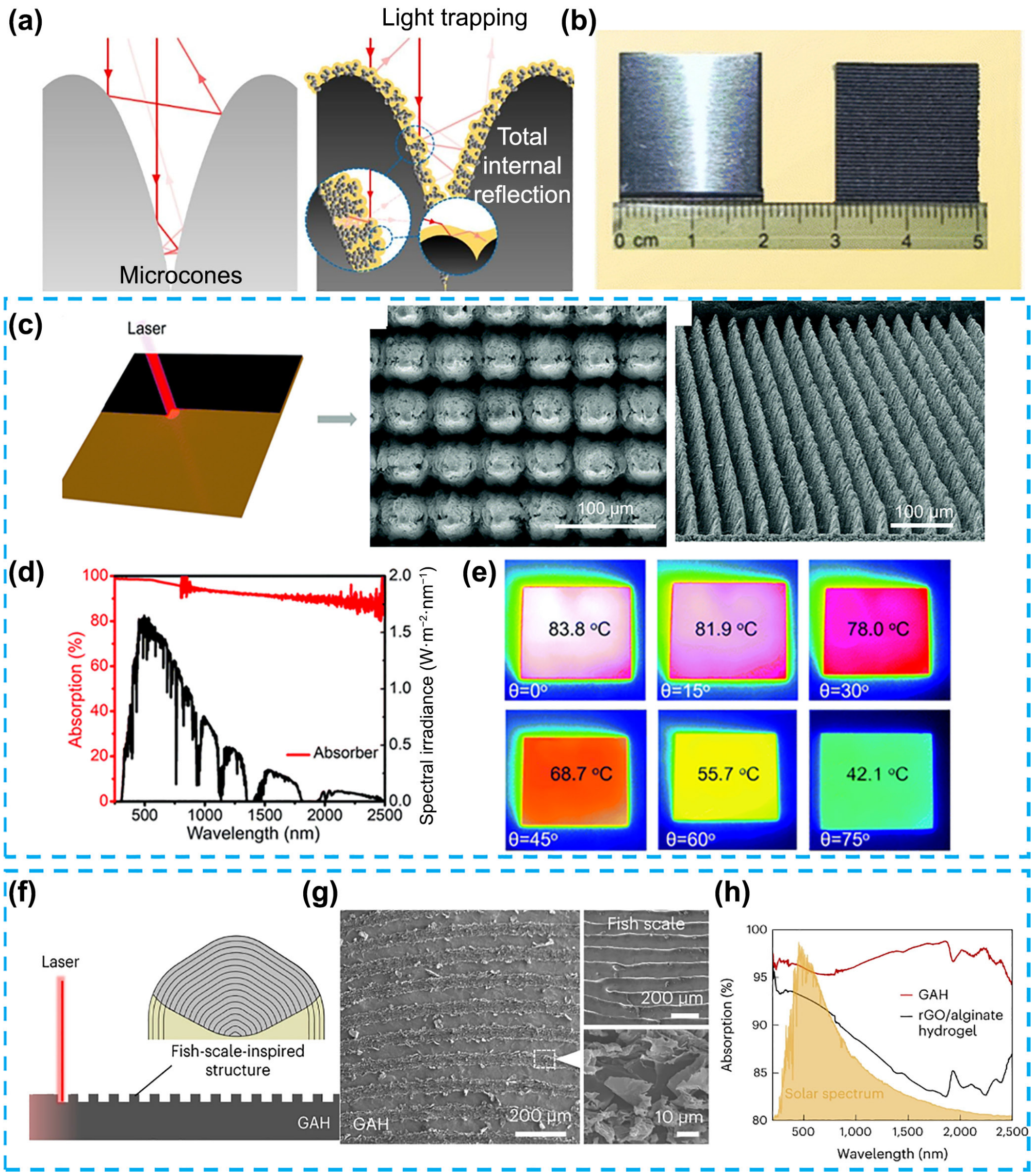

Figure 5 (a) Schematic diagram of the optical trap effect. Reproduced with permission from Ref. [70], © Elsevier B.V. 2022. (b) Comparison of samples before and after laser processing of Al foil. Reproduced with permission from Ref. [71], © The Royal Society of Chemistry 2023. (c) Fabrication and morphological analysis of the micro-pyramid array. (d) Ultraviolet–visible-near infrared spectrum of the solar absorption surface of the micro-pyramid array. (e) Infrared images of the micro-pyramid array under standard sunlight at different angles of incidence. Reproduced with permission from Ref. [72], © The Royal Society of Chemistry 2021. (f) Schematic design of biomimetic fish scales. (g) Surface morphology of GAH and real fish scales. (h) Ultraviolet–visible-near infrared spectra of GAH (red curve) and rGO/alginate hydrogel without fish scale pattern (black curve). Reproduced with permission from Ref. [73], © Hao, X. et al. 2023.

interface. By constructing a heterostructure (Janus–S) on an Al substrate, the photothermal interface is physically decoupled from the water supply pathway; decoupling the photothermal interface from the water supply pathway can effectively address the mutual interference between evaporation and solar absorption observed in conventional systems [72, 77]. The water supply function can be achieved through capillary action on the supply side, demonstrating effective transmission performance in both horizontal and vertical directions [77] (Fig. 6(e)). Owing to its excellent water transport properties and the design of heterogeneous structures, the evaporator demonstrates a high evaporation rate as well as outstanding long-term stability.

In brief, the laser etching technique mainly creates micro-nano structures on metal substrates. By leveraging the optical trapping effect, the surface plasmon effect is enhanced, achieving excellent photothermal conversion efficiency. Furthermore, it can also enhance the wetting property of the material surface and improve the water transmission capacity, leading to a substantial acceleration in water evaporation rates. In addition to metal substrates, lasers can also process polymeric materials, thereby imparting them with excellent photothermal conversion properties.

4 Application of laser-induced graphene in SDIE

Since the inception of LIG technology in 2014 [24], it has garnered significant interest from the research community owing to its

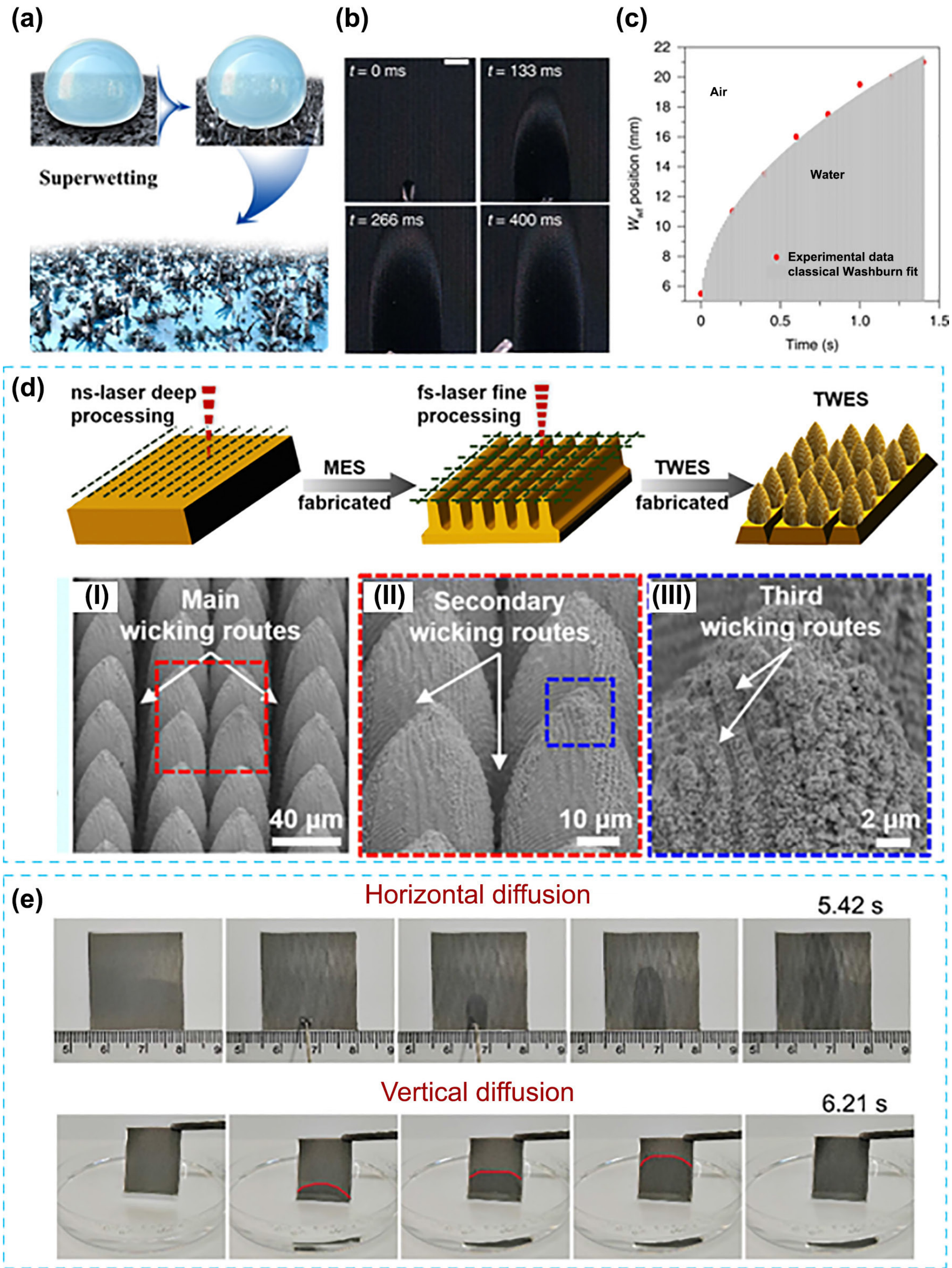

Figure 6 (a) Schematic diagram of a superhydrophilic surface. Reproduced with permission from Ref. [75], © American Chemical Society 2025. (b) Capillary action of a water droplet on the evaporator surface. (c) Relationship between water wet front (W_{wf}) propagation and time, fitted with Washburn. Reproduced with permission from Ref. [66], © Singh, S. C. et al. 2020. (d) Schematic diagram of the TWES manufacturing process and surface microstructure morphology. Reproduced with permission from Ref. [76], © The Royal Society of Chemistry 2023. (e) Digital photographs of water transport on the surface of Janus–S placed horizontally and vertically. Reproduced with permission from Ref. [77], © Elsevier B.V. 2025.

simplicity and patternable to graphene fabrication [78–81] (Fig. 4(b)). Advancements in this technology have extended the range of applicable substrates beyond polyimide (PI) to include various polymeric materials, such as polyethersulfone (PES) [82, 83], phenolic resin [84, 85], aramid fibers [86, 87], lignin [88, 89], wood [90, 91], and others [92]. This diversification of substrates has substantially expanded the scope of LIG applications, with numerous studies demonstrating its successful implementation in areas, including energy storage [15, 79], flexible electronics [18, 80], and photoelectric sensors [16]. This chapter specifically examines the application of LIG within SDIE.

LIG technology employs high-pulse energy to directly irradiate carbonizable substrates, inducing carbonization or chemical reduction on the substrate surface, thereby generating graphene and its derivatives [78]. Owing to the abundant π–π stacking interactions present in carbon-based materials, the bandgap between the HOMO and the LUMO is effectively reduced, resulting in superior photothermal conversion performance. As a result, these materials have been widely utilized in SDIE [40]. The LIG technique enables not only the fabrication of photothermal materials but also the *in-situ* construction of porous surface structures. These porous surfaces reduce energy loss due to light diffuse reflection and substantially enhance the evaporation area, they can significantly enhance the rate of water evaporation [93] (Fig. 7(a)).

In addition, laser processing carried out on different substrates can result in the creation of photothermal materials with unique properties. For instance, LIG fabricated on hydrophobic substrates exhibits hydrophobic characteristics, whereas LIG produced on hydrophilic substrates demonstrates hydrophilicity. The preparation of hydrophobic LIG on PI films, with the underside subjected to hydrophilic treatment; this structure enables the film evaporator to stably float on the water surface like a lotus leaf [94] (Fig. 7(b)). The LIG formed on the hydrophobic polybenzoxazine resin (poly(Ph-ddm)) exhibits superhydrophobic properties [95] (Fig. 7(c)). When combined with a forest-like structural design, this material achieves a high solar absorption rate of 99.0%, along with notable salt resistance and excellent acid-base durability. Similarly, asymmetric laser-induced treatment on both sides of a wooden block results in differing hydrophobic and hydrophilic properties on the upper and lower surfaces, respectively, thereby facilitating functions, such as salt resistance and antibacterial purification [96] (Fig. 7(d)). This layered design achieves a solar energy conversion efficiency of 110%, with removal rates of ≥ 99.9% for metal ions and ≥ 90% for lipophilic contaminants, while maintaining stable operation even under high salinity conditions.

LIG technology facilitates the design of both specific microstructures and macroscopic structures. The interaction between an infrared laser and the processed material generates a non-uniform distribution of thermal stress, which leads to material curling. By making rational use of this phenomenon, it is possible to fabricate three-dimensional (3D) LIG with specialized geometries *in-situ*, as demonstrated by arched evaporators (Fig. 8(a)). The integration of its macroscopic arched architecture with a grass-like microstructure significantly enhances the rate of water evaporation. LIG can be fabricated using various flexible substrates, allowing for the design of multiple 3D structures aimed at inhibiting salt crystallization or directing salt deposition. For instance, LIG was fabricated on hydrophilic cotton fabric, and a 3D wavy structure was engineered such that its lower section maintained close contact with the wick layer [29]. This design facilitated the diffusion of high concentrations of salt ions from the LIG into the seawater, thereby ensuring that the salt concentration within the LIG remained below the crystallization threshold (Fig. 8(b)). This design endowed the device with a high salt resistance stability, enabling continuous operation for 13 h without salt crystallization (Fig. 8(c)). Although salt crystals may form on the surface, they can be rapidly dissolved when subjected to dark conditions (Fig. 8(c)). Alternatively, a superhydrophilic conical structure (SCE) can be designed (Fig. 8(d)), which enables selective salt crystallization at the apex of the cone (Fig. 8(e)). This ingenious design facilitates salt collection without compromising the evaporation rate [98].

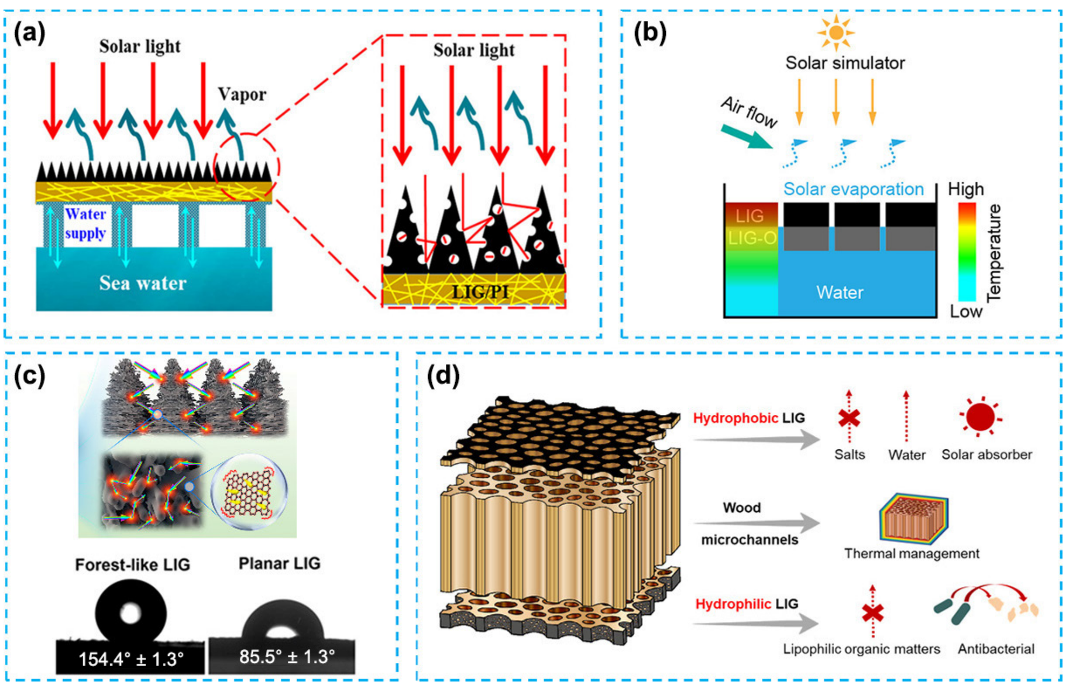

Figure 7 (a) Schematic diagram of seawater desalination using LIG/PI membrane via interfacial evaporation. Reproduced with permission from Ref. [93], © American Chemical Society 2020. (b) Schematic diagram of a self-floating solar interfacial evaporation system. Reproduced with permission from Ref. [94], © American Chemical Society 2020. (c) Forest-like graphene film structure, broadband solar absorption, and theoretical mechanism of high photothermal conversion, along with water contact angle measurements. Reproduced with permission from Ref. [95], © American Chemical Society 2021. (d) Schematic diagram of the SDIE system based on wood. Reproduced with permission from Ref. [96], © American Chemical Society 2020.

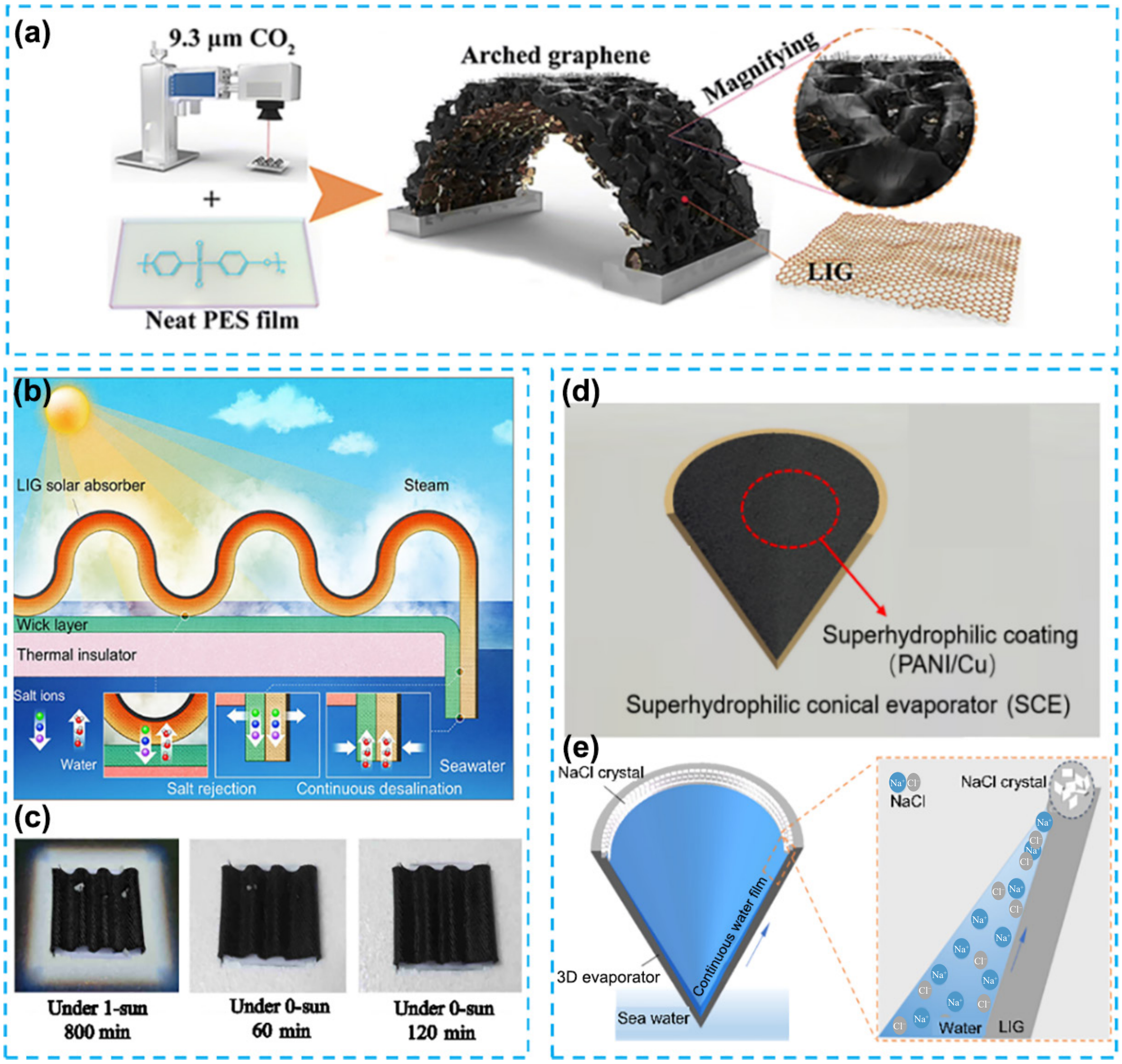

Figure 8 (a) Schematic of CO_2 pulsed laser fabrication of arched graphene on PES film. Reproduced with permission from Ref. [97], © The Royal Society of Chemistry 2025. (b) Schematic diagram of the working principle of the 3D LIG evaporator (LIGE) for efficient solar seawater desalination. (c) Demonstration of the salt rejection capability and self-cleaning performance of the 3D LIGE. Reproduced with permission from Ref. [29], © American Chemical Society 2024. (d) Schematic diagram of the SCE structure. (e) Illustration of the directional salt crystallisation in the SCE. Reproduced with permission from Ref. [98], © Elsevier B.V. 2025.

In the domain of seawater desalination, the removal of pollutants from water represents a critical challenge. The surface of LIG can be functionalized with various materials to facilitate catalytic degradation or adsorption of wastewater [31, 83, 99, 100]. Titanium dioxide (TiO_2) can be doped into LIG (Fig. 9(a)). The LIG facilitated the rapid migration of photogenerated electrons, effectively inhibiting the recombination of charge carriers, which in turn substantially enhanced the photocatalytic efficiency of the composite material [30]. Consequently, the LIG/TiO_2 composite demonstrated not only a high evaporation rate of 2.13 $kg \cdot m^{-2} \cdot h^{-1}$ but also superior degradation performance toward organic pollutants, achieving degradation efficiencies of 98.3% and 97.8% for methylene blue (MB) and rhodamine B, respectively (Figs. 9(b) and 9(c)). In addition to the incorporation of catalysts, continuous metal–organic framework (MOF) nanolayers can be synthesized on the surface of LIG, resulting in the formation of hierarchical micro-nano composite membranes with selective sieving capabilities (multilevel cellular graphene skeleton (MCGK)/zeolitic imidazolate framework-8 (ZIF-8)) (Fig. 9(d)). During the process of water evaporation, these membranes effectively remove volatile organic compounds (VOCs) (Fig. 9(e)) and metal ions (Fig. 9(f)) [28].

Recent years have witnessed a growing interest in the extraction of resources from seawater, with lithium extraction technology emerging as particularly strategic [101]. Incorporating MOF (HKUST-1) material beneath LIG can also facilitate the extraction of lithium ions (Fig. 10(a)). By leveraging the size effect, HKUST-1 selectively separates Li^+ from Mg^{2+}, enabling Li^+ to penetrate the interior of LIG. After multiple evaporation extraction cycles, high-purity lithium salts can be obtained [34] (Fig. 10(b)).

The integration of photothermal water evaporation with clean energy production has significantly improved the efficiency of solar energy utilization [9, 102, 103]. By preparing LIG on substrates with hydrovoltaic effect, such as basswood [104], electricity can be generated during the process of interface evaporation (Fig. 10(c)). It is also possible to load materials on the LIG surface that can promote the ion–electron conversion, thereby enhancing the

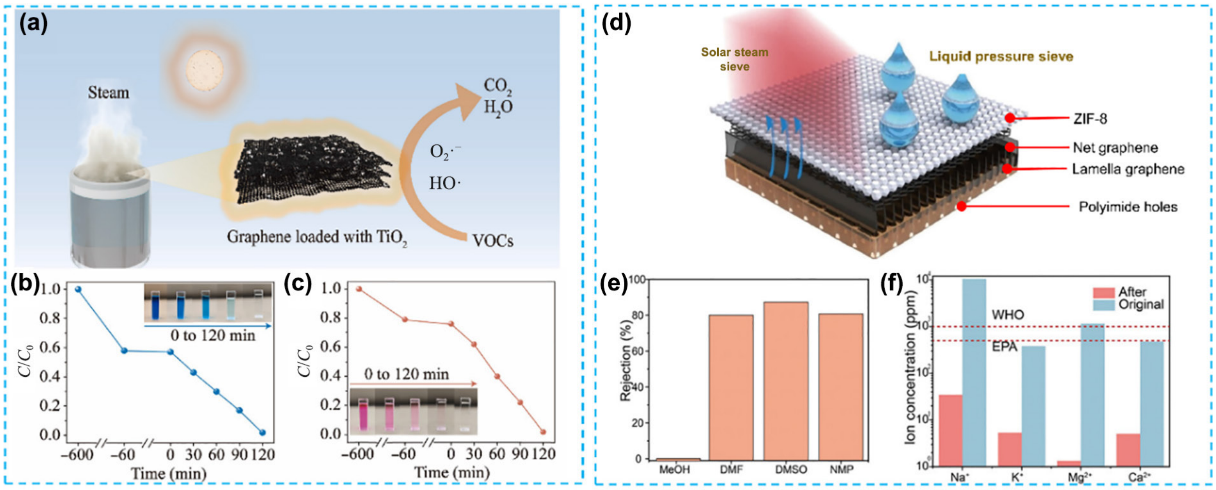

Figure 9 Water purification applications based on LIG. (a) Schematic diagram of photothermal evaporation-photocatalysis. ((b) and (c)) Relative concentration change curves of methylene blue and rhodamine B with illumination time. Reproduced with permission from Ref. [30], © Elsevier B.V. 2025. (d) Schematic diagram of a multiphase water molecular sieve. (e) VOC rejection performance of MCGK/ZIF-8 membrane for aqueous solutions of methanol (MeOH), N,N-dimethylformamide (DMF), dimethyl sulfoxide (DMSO), and N-methyl-2-pyrrolidone (NMP). (f) Comparison of ion concentrations after seawater desalination using MCGK/ZIF-8. Reproduced with permission from Ref. [28], © Zhang, S. et al. 2023.

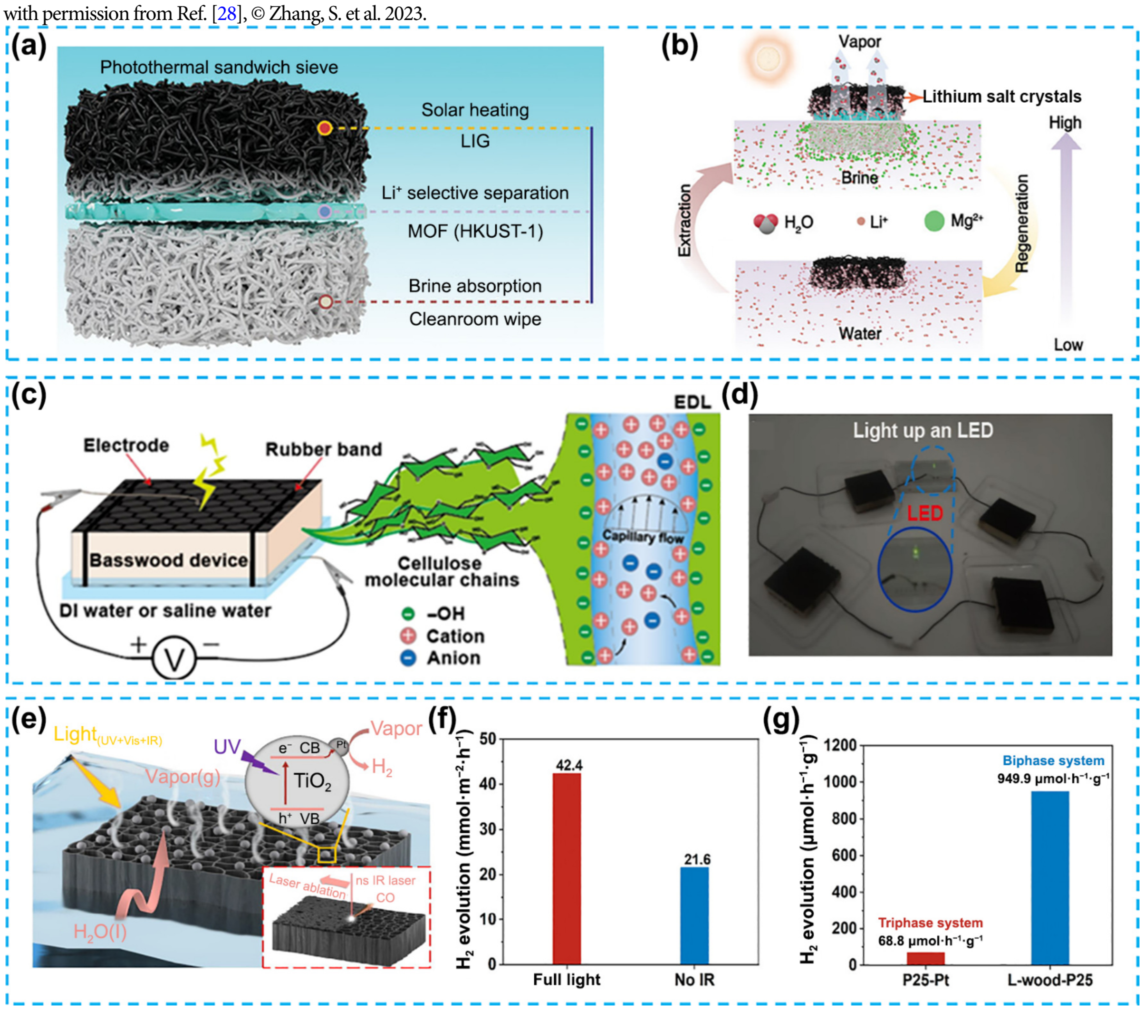

Figure 10 illustrates LIG-loaded functional materials utilized for clean energy production. (a) Schematic diagram of the sandwich structure of the solar-driven lithium extraction device. (b) Schematic of the lithium extraction and regeneration process in the solar-driven device. Reproduced with permission from Ref. [34], © Wiley-VCH GmbH 2024. (c) Schematic diagram of the water evaporation-induced power generation mechanism. (d) Digital photograph of four devices connected in series, lighting a light-emitting diode. Reproduced with permission from Ref. [104], © Elsevier Ltd. 2025. (e) Schematic of photothermal evaporation coupled with photocatalytic hydrogen production. (f) Comparison of hydrogen production rates of L-wood-P25 before and after filtering the infrared light spectrum. (g) Comparison of hydrogen evolution rates between the triphasic P25-Pt system and the biphasic photothermal-photocatalytic L-wood-P25 system. Reproduced with permission from Ref. [32], © American Chemical Society 2025.

hydrovoltaic effect [104]. Moreover, multiple evaporators can be connected in series to drive electronic components (Fig. 10(d)).

In addition to electrical energy, hydrogen energy is also an important clean energy source. Loading photocatalysts on the surface of LIG can also promote the photocatalytic hydrogen evolution [32] (Fig. 10(e)): Firstly, LIG can increase the migration rate of photogenerated carriers and inhibit the recombination of photogenerated holes and electrons. Secondly, this system can directly catalyze water vapor into hydrogen gas, which has a lower Gibbs free energy compared to liquid-phase catalysis [105] (Fig. 10(g)). Thirdly, the higher temperature at the photothermal interface can promote the photocatalytic hydrogen evolution reaction (Fig. 10(f)). This resulted in achieving a hydrogen production rate of 42.4 mmol·m^{-2}·h^{-1} and a water evaporation rate of 4.809 kg·m^{-2}·h^{-1} without the need to add a sacrificial agent.

In comparison to laser etching technology, LIG technology demonstrates a broader applicability across diverse materials, facilitating a greater variety of structural configurations and functional enhancements. The researchers utilized the diversity of laser chemistry to couple other chemical reactions on the basis of preparing LIG, and finally obtained carbon-based semiconductor composite materials.

5 Application of laser *in-situ* synthesis LIG/composite materials in SDIE

Due to the variety of photochemical reactions, lasers are capable of producing not only graphene but also graphene-based composites, such as LIG/semiconductors [106], LIG/metal oxides [108–110], and LIG/metal carbides [107] (Fig. 4(c)). The doped materials increase the number of adsorption sites within the porous structure of LIG, thereby enabling efficient purification of contaminated water. *In-situ* synthesized rGO/copper sulfide (rGO/CuS) composites (Fig. 11(a)) [106]. CuS nanoparticles inhibit the restacking of rGO nanosheets, facilitate the development of mesopores, and significantly enhance the specific surface area of rGO. This structural modification facilitates the effective adsorption of rhodamine B and volatile m-dinitrobenzene during the water

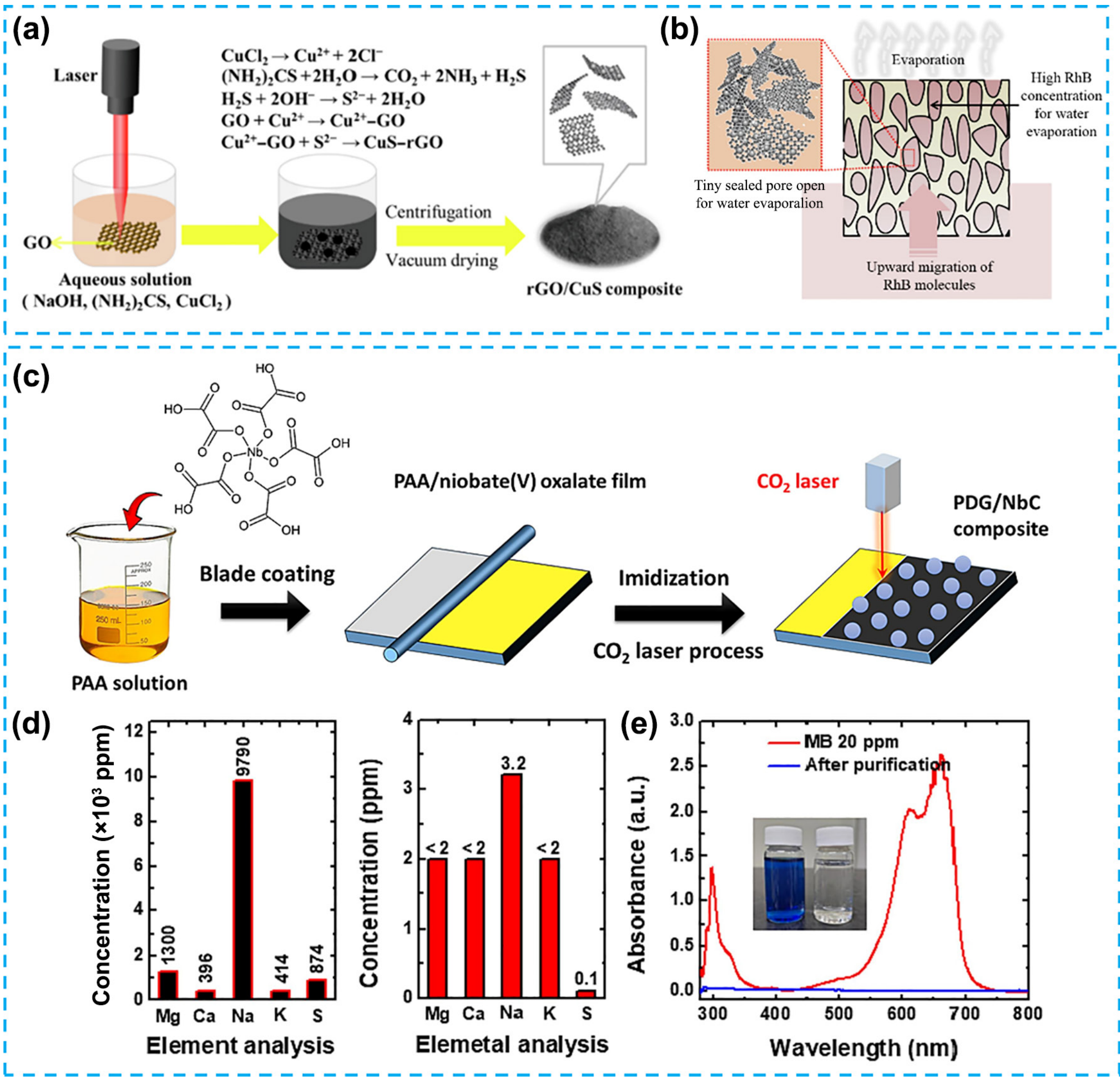

Figure 11 (a) Schematic diagram of the laser synthesis of rGO/CuS nanocomposite. (b) Schematic diagram of rhodamine B adsorption by melamine sponge (MS) loaded with rGO/CuS. Reproduced with permission from Ref. [106], © Elsevier B.V. 2022. (c) Schematic diagram of the preparation of NbC-PDG composite. (d) Concentration of metal ions before and after seawater desalination. (e) Absorbance spectra of raw wastewater and purified MB solution (inset: MB solutions before and after purification). Reproduced with permission from Ref. [107], © Elsevier B.V. 2024.

evaporation process (Fig. 11(b)). A similar compound of NbC and polyimide-derived graphene (NbC-PDG) [107] (Fig. 11(c)), not only exhibits superior retention of various metal ions (Fig. 11(d)) but also can effectively remove methylene blue dye (Fig. 11(e)), demonstrating significant potential in the field of water purification.

As an advanced derivative of LIG, *in-situ* synthesized LIG composites possess significant potential for further development. To date, enhancements in composite materials have primarily focused on improving the adsorption capabilities of LIG. The *in-situ* synthesis of photothermal-photocatalytic materials within these composites would represent a pioneering advancement in the field. The above laser processing techniques are all applied to solid substrates. Next, we will introduce the laser processing technology in the liquid phase: liquid-phase pulsed ablation.

6 Application of laser liquid phase pulsed ablation process in SDIE

Liquid-phase pulsed laser ablation, which emerged in the 1990s [111], has been extensively employed for the synthesis of diverse nanomaterials [112, 113]. In liquid media, the absorption of laser energy by molecules can exceed the binding energy of valence electrons, leading to the generation of highly excited free radicals and solvated electrons, which subsequently trigger chemical reactions. These laser-induced chemical reactions occur uniformly under specific conditions and kinetic parameters, yielding distinctive products. By positioning a solid target within the liquid and focusing the laser beam at the liquid-target interface, nanoparticles are generated (Fig. 4(d)), typically exhibiting good dispersion within the liquid [114]. This technique is versatile and can be readily applied to produce a wide range of materials, including pure metals, semiconductors [115, 116], dielectric nanoparticles [117, 118], and advanced composite nanomaterials [119–121] with complex multi-element architectures. These materials can also be applied in the field of SDIE.

Gurbatov et al. utilized the liquid-phase pulsed ablation technique to fabricate amorphous TiO_2 nanospheres modified with Au nanoclusters (Au@TiO_2) (Fig. 12(a)). This laser treatment induced a reduction in the bandgap of the amorphous TiO_2. Combined with the plasmonic resonance effect of the surface-modified Au nanoclusters, the Au@TiO_2 exhibited pronounced solar absorption across the visible and near-infrared spectral regions, with an average absorption of approximately 96% [122]. Under simulated solar irradiation, its photothermal performance contrasts sharply with that of untreated TiO_2 (Fig. 12(b)). This method can also produce rutile TiO_2 nanoparticles with abundant oxygen vacancies (L-TiO_2) (Fig. 12(c)). The existence of oxygen vacancies was shown to decrease the bandgap (Fig. 12(d)), consequently leading to a substantial improvement in solar absorption and photothermal conversion efficiency [39]. The L-TiO_2 material was subsequently integrated onto nickel foam to construct a self-floating evaporator (Fig. 12(e)). This device demonstrated a water evaporation rate of 1.25 $kg \cdot m^{-2} \cdot h^{-1}$ and exhibited a photothermal evaporation efficiency of 78.5% under standard solar irradiation conditions.

The photothermal nanofluid synthesized via the liquid-phase pulsed ablation technique can uniformly heat bulk water and facilitate efficient water evaporation. However, compared to interfacial evaporation, bulk-water heating demonstrates certain limitations. Although SDIE devices are assembled through post-

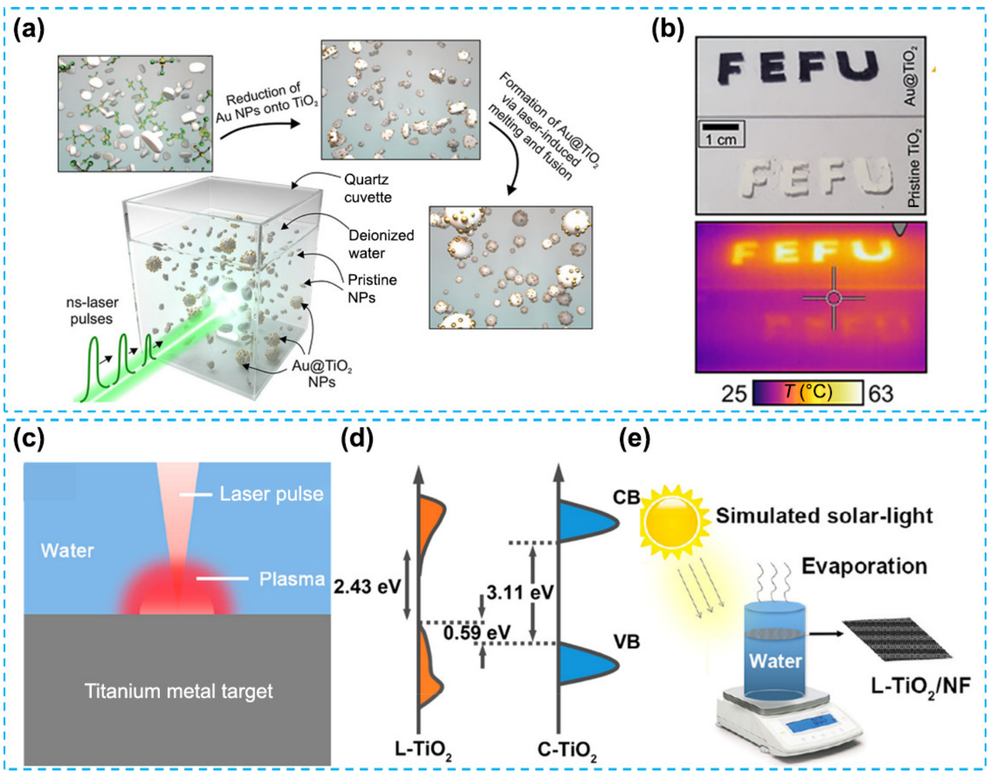

Figure 12 (a) Schematic representation of the laser ablation process employed for the synthesis of Au@TiO_2 nanoparticles in a liquid medium. (b) Optical and infrared imaging of Au@TiO_2 nanoparticles and TiO_2 subjected to simulated sunlight irradiation. Reproduced with permission from Ref. [122], © American Chemical Society 2021. (c) Schematic diagram of preparing L-TiO_2 by laser ablation technology. (d) Energy band diagrams of L-TiO_2 and C-TiO_2. (e) Schematic diagram of solar-driven water evaporation measurement. Reproduced with permission from Ref. [39], © American Chemical Society 2020.

processing methods, their efficiency of solar-to-steam conversion possesses significant potential for enhancement. Notably, due to the diversity of photochemical reactions, this technology offers expanded potential applications.

7 Summary and prospects

Laser processing technology has been widely utilized within the field of SDIE, as summarized in Table 1. This review focuses on

Table 1 Summary of reports on laser processing techniques in SDIE

Serial	Laser processing technology	Substrate	Solar absorption	The rate of water evaporation (kg·m^{-2}·h^{-1})	Function	References
1	Laser etching	Al	95.50%	2.59	Desalination	[123]
2		Al	97%	3.76	Thermoelectric generator	[33]
3		Al	99%	3.5	Desalination	[124]
4		Al	97%	1.5	Desalination	[66]
5		Cu	96%	2.21	Condensate collection	[72]
6		Cu	—	3.33	Desalination	[76]
7		Ti foam	97%	1.79	Desalination	[125]
8		N-graphene	—	1.77	Desalination	[75]
9		GO/SA	95%	2.51	Antibacterial + wastewater treatment	[73]
Advantage: (1) wide applicability of materials and (2) preparation of materials with high solar absorption.						
10	Laser induced graphitization	PI film	98%	1.42	Desalination	[93]
11		PI film	90.50%	1.512	Desalination	[94]
12		PI film	93%	2.83	Desalination	[126]
13		PI film	97%	1.31	Desalination	[127]
14		PI/LIG + MOF	97%	2.26	Lithium extraction	[34]
15		PI/LIG + Cu	96%	2.25	Directional salt crystallization	[98]
16		PES	—	2.82	Wastewater treatment + desalination	[83]
17		Poly(Ph-ddm)	99%	1.22	Desalination	[95]
18		Polypropylene	—	1.93	Wastewater treatment	[100]
19		Kevlar fabrics	97%	1.608	Antibacterial	[128]
20		Cellulose aerogel	95.20%	1.9	Desalination	[99]
21		Cotton paper	98.50%	1.7	Desalination	[129]
22		Wood/LIG + MOF	92%	2.66	Hydropower + desalination	[130]
23		Wood	—	1.6	Wastewater treatment + antibacterial	[96]
24		Lignin hydrogel	90%	2.33	Hydrovoltaic generation	[102]
25		Glass fibre + GO	93%	2.06	Oil–water separation	[31]
26		Biomass porous carbon	95%	1.74	Desalination	[131]
Advantage: (1) highly versatile and capable of expansion, (2) wide range of materials applicable, and (3) preparation of materials with high solar absorption.						
27	Laser *in-situ* synthesis of LIG/composite materials	GO + $CuCl_2$	—	2.09	Wastewater treatment	[106]
28		PI + $Nb(HC_2O_4)_5$	—	0.7	Wastewater treatment	[107]
29		PI + $CuCl_2$	98.91%	2.54	Desalination	[108]
30		Cellulose paper + $Co(NO_3)_2$ + gelatin	90.80%	1.5	Wastewater treatment	[109]
31		Cellulose paper + tannic acid-iron complex	93.28	1.82	Desalination	[110]
Advantage: (1) *in-situ* preparation of integrated multi-functional materials and (2) highly versatile and capable of expansion.						
32	Laser liquid phase ablation	TiO_2	87.9%	1.25	Desalination	[39]
33		$HAuCl_4$ + TiO_2	96%	2.5	—	[122]
34		Te foil	85%	1.1	—	[132]
Advantage: (1) controllable nanostructure morphology.						

four principal techniques: laser etching, laser-induced graphene formation, laser *in-situ* synthesis of LIG/composite materials, and liquid-phase pulsed ablation, along with their corresponding applications in this area. Overall, the laser etching process can precisely and eco-friendly fabricate photothermal materials as well as surface modification; this method is associated with relatively high processing costs, susceptibility of the photothermal layer to wear, and limited capacity for multifunctional integration, restricting its applicability primarily to seawater desalination. Conversely, LIG technology offers a wide range of material options and features a process that is both convenient and efficient. Moreover, LIG exhibits significant potential for multifunctional integration, making it suitable for diverse applications, such as seawater desalination, wastewater treatment, clean energy generation, and resource recovery (Table 1). Laser *in-situ* synthesis of LIG/composite materials can *in-situ* synthesize carbon-based semiconductor composites. However, the process is more complex than LIG, and the applicable materials have certain limitations, thereby narrowing their application scope. Its use is primarily confined to seawater desalination and wastewater treatment. Additionally, liquid-phase pulse ablation technology can produce nanofluids with high purity and excellent dispersion. Despite these advantages, the process is complex, and the resulting product exhibits poor size uniformity. Consequently, there remains considerable potential for enhancement in its practical application.

Laser processing technology presents three significant advantages in the application of photothermal water evaporation:

(1) Laser processing technology enables precise fabrication of photothermal layers, allowing not only the construction of microstructures but also the control of the photothermal layer thickness, thereby achieving precise thermal localization design.

(2) Laser processing technology demonstrates extensive compatibility and adaptability in its combined application with various materials, enabling the selection of materials optimized for specific application contexts. Moreover, it can be combined with various functional materials to achieve multifunctional integration, with applications that include wastewater treatment, renewable energy generation, and resource recycling.

(3) The diversity of laser chemistry enables the *in-situ* generation of composite materials possessing multiple functionalities.

This field remains rich with potential for further development. Here, we propose the following possible research directions for future reference:

(1) Both laser etching technology and LIG technology face challenges concerning the mechanical abrasion and material detachment of microstructures or photothermal coatings formed on material surfaces. This issue remains unresolved, thereby requiring further research to achieve a comprehensive solution.

(2) Integrating laser processing with machine learning for adaptive optimization in the design of evaporator structures and materials.

(3) Mechanistic investigation: How can ultrafast laser *in-situ* characterization techniques be employed to perform real-time analysis of the microscopic mechanisms governing water and heat transfer during the interfacial evaporation process?

In conclusion, this work provides a systematic review of the application of laser processing technology in SDIE. Laser processing technology improves photothermal conversion efficiency through three primary approaches: fabricating microstructures on material surfaces, directly carbonizing the material and modulating the band gap of semiconductor materials. Creating microstructures that enhance hydrophilicity and capillary effect, thereby facilitating water transport. Currently, laser micro-nano processing technology has been effectively applied in SDIE; nevertheless, it is constrained by certain limitations. Conversely, laser chemical synthesis holds significant promise for future advancement. This review aims to support the progression of laser processing technologies within the context of SDIE.

Data availability

Not applicable.

Acknowledgements

This work was supported by the National Key R&D Program of China (No. 2024YFF0506000) and the National Natural Science Foundation of China (Nos. 52350362 and T2596012).

Declaration of competing interest

All the contributing authors report no conflict of interests in this work.

Author contribution statement

Z. H. Y.: Writing manuscript, data curation and check; Z. H. S. and Y. F. Z.: Data curation and literature collection; J. H. Z. and B. W.: Take part in the discussion and organize the logic; F. Z. and Y. Z.: Project administration; H. H. C., L. J., and L. T. Q.: Check and correct. All the authors have approved the final manuscript.

Use of AI statement

None.

References

[1] Chu, S.; Majumdar, A. Opportunities and challenges for a sustainable energy future. *Nature* **2012**, *488*, 294–303.

[2] Liu, B. W.; Yang, Y. W.; Zhao, Q.; Liu, Y. H.; Shen, Y. Y.; Ma, Y.; Que, W. X. The route for applied interfacial solar vapor generation: Fundamental principles, device design, and practical application. *Energy Environ. Sci.* **2025**, *18*, 6366–6437.

[3] Qiblawey, H. M.; Banat, F. Solar thermal desalination technologies. *Desalination* **2008**, *220*, 633–644.

[4] Kaushal, A.; Varun. Solar stills: A review. *Renew. Sustain. Energy Rev.* **2010**, *14*, 446–453.

[5] Ghasemi, H.; Ni, G.; Marconnet, A. M.; Loomis, J.; Yerci, S.; Miljkovic, N.; Chen, G. Solar steam generation by heat localization. *Nat. Commun.* **2014**, *5*, 4449.

[6] Chen, X. Y.; Ye, Q.; Shi, C. M.; Zhang, L. W.; Zhou, P.; Chen, M. J. Understanding solar thermal gradient to improve solar evaporation performance for water collection. *Nano Res. Energy* **2025**, *4*, e9120152.

[7] Wei, Z. C.; Wang, J.; Guo, S.; Tan, S. C. Towards highly salt-rejecting solar interfacial evaporation: Photothermal materials selection, structural designs, and energy management. *Nano Res. Energy* **2022**, *1*, 9120014.

[8] Deng, Z. Y.; Zhou, J. H.; Miao, L.; Liu, C. Y.; Peng, Y.; Sun, L. X.; Tanemura, S. The emergence of solar thermal utilization: Solar-driven steam generation. *J. Mater. Chem. A* **2017**, *5*, 7691–7709.

[9] Li, X. M.; Feng, G.; Chen, Y. D.; Li, J. D.; Yin, J.; Deng, W.; Guo, W. L. Hybrid hydrovoltaic electricity generation driven by water evaporation. *Nano Res. Energy* **2024**, *3*, e9120110.

[10] Wang, Y. D.; Hu, J. Q.; Yu, L.; Wu, X.; Zhang, Y. Y.; Xu, H. L. Recent strategies for constructing efficient interfacial solar evaporation systems. *Nano Res. Energy* **2023**, *2*, e9120062.
[11] Zhang, P. P.; Wang, H. Y.; Wang, J.; Ji, Z. Y.; Qu, L. T. Boosting the viable water harvesting in solar vapor generation: From interfacial engineering to devices design. *Adv. Mater.* **2024**, *36*, 2303976.
[12] Kim, H. T.; Philip, L.; McDonagh, A.; Johir, M.; Ren, J. W.; Shon, H. K.; Tijing, L. D. Recent advances in high-rate solar-driven interfacial evaporation. *Adv. Sci.* **2024**, *11*, 2401322.
[13] Tan, P. X.; Wang, C. B.; Wei, D.; Wang, F.; Zhao, Z. X.; Zhang, W. H. Laser processing materials for photo-to-thermal applications. *Adv. Colloid Interface Sci.* **2025**, *337*, 103382.
[14] Zhang, P. P.; Liao, Q. H.; Yao, H. Z.; Huang, Y. X.; Cheng, H. H.; Qu, L. T. Direct solar steam generation system for clean water production. *Energy Storage Mater.* **2019**, *18*, 429–446.
[15] Zhao, Y. F.; Luo, M.; Hu, Y. J.; Cheng, H. H.; Yan, J. F.; Jiang, L.; Qu, L. T. Laser micro/nano fabrication of electrochemical filtering capacitors: Multiscale structural engineering for high-frequency power conditioning. *Adv. Energy Mater.* **2025**, *15*, e02620.
[16] Wang, Y.; Zhao, Y.; Li, X.; Jiang, L.; Qu, L. T. Laser-based growth and treatment of graphene for advanced photo-and electro-related device applications. *Adv. Funct. Mater.* **2022**, *32*, 2203164.
[17] Xiao, C. C.; Feng, J.; Xu, H. R.; Xu, R.; Zhou, T. Scalable strategy to directly prepare 2D and 3D liquid metal circuits based on laser-induced selective metallization. *ACS Appl. Mater. Interfaces* **2022**, *14*, 20000–20013.
[18] Le, T. S. D.; Phan, H. P.; Kwon, S.; Park, S.; Jung, Y.; Min, J.; Chun, B. J.; Yoon, H.; Ko, S. H.; Kim, S. W. et al. Recent advances in laser-induced graphene: Mechanism, fabrication, properties, and applications in flexible electronics. *Adv. Funct. Mater.* **2022**, *32*, 2205158.
[19] Chu, G. L.; Zhang, Y. Y.; Zhou, Z. R.; Zeng, W. X.; Chen, D. F.; Yu, S. P.; Wang, J. M.; Guo, Y. M.; Sun, X.; Li, M. Rapid CO_2-laser scribing fabrication of an electrochemical sensor for the direct detection of Pb^{2+} and Cd^{2+}. *Nano Res.* **2023**, *16*, 7671–7681.
[20] Xu, X. B.; Dong, Y. H.; Zhang, Y. Z.; Han, Z. Y.; Liu, J. X.; Yu, D. J.; Wei, Y.; Zou, Y. S.; Huang, B.; Chen, J. et al. High-definition colorful perovskite narrowband photodetector array enabled by laser-direct-writing. *Nano Res.* **2022**, *15*, 5476–5482.
[21] Feng, Y. S.; Liang, M. S.; You, R.; Li, T. S.; Zhu, L. Q. Femtosecond laser fabrication of noble metal plasma nanostructures and its application—A mini review. *Front. Phys.* **2022**, *10*, 918372.
[22] Clerici, F.; Fontana, M.; Bianco, S.; Serrapede, M.; Perrucci, F.; Ferrero, S.; Tresso, E.; Lamberti, A. *In-situ* MoS_2 decoration of laser-induced graphene as flexible supercapacitor electrodes. *ACS Appl. Mater. Interfaces* **2016**, *8*, 10459–10465.
[23] Deng, H.; Zhang, C.; Xie, Y. C.; Tumlin, T.; Giri, L.; Karna, S. P.; Lin, J. Laser induced MoS_2/carbon hybrids for hydrogen evolution reaction catalysts. *J. Mater. Chem. A* **2016**, *4*, 6824–6830.
[24] Lin, J.; Peng, Z. W.; Liu, Y. Y.; Ruiz-Zepeda, F.; Ye, R. Q.; Samuel, E. L. G.; Yacaman, M. J.; Yakobson, B. I.; Tour, J. M. Laser-induced porous graphene films from commercial polymers. *Nat. Commun.* **2014**, *5*, 5714.
[25] Wang, H. M.; Deng, D. X.; Zhai, Z. J.; Yao, Y. X. Laser-processed functional surface structures for multi-functional applications—A review. *J. Manuf. Process.* **2024**, *116*, 247–283.
[26] Arciniegas, M. P.; Castelli, A.; Piazza, S.; Dogan, S.; Ceseracciu, L.; Krahne, R.; Duocastella, M.; Manna, L. Laser-induced localized growth of methylammonium lead halide perovskite nano- and microcrystals on substrates. *Adv. Funct. Mater.* **2017**, *27*, 1701613.
[27] Park, H.; Park, J. J.; Bui, P. D.; Yoon, H.; Grigoropoulos, C. P.; Lee, D.; Ko, S. H. Laser-based selective material processing for next-generation additive manufacturing. *Adv. Mater.* **2024**, *36*, 2307586.
[28] Zhang, S. Z.; Yuan, J.; Wang, S.; Li, Y. F.; Xu, Y. H.; Sun, D. Y.; Liu, F.; Cheng, G. J. Synergistic multilevel sieving membranes: Integrating cellular graphene skeleton with continuous MOFs nanolayer for superior multiphase water separation. *Adv. Funct. Mater.* **2024**, *34*, 2307571.
[29] Le, T. S. D.; Yang, D.; Nam, H. K.; Lee, Y.; Lim, C. T.; Lee, B. J.; Kim, S. W.; Kim, Y. J. Low-cost, eco-friendly, and high-performance 3D laser-induced graphene evaporator for continuous solar-powered water desalination. *ACS Nano* **2024**, *18*, 33220–33231.
[30] Zhong, H.; Lai, Z. Y.; Xu, D.; Wang, S. F. Highly pure water generation via solar driven evaporation and photodegradation based on laser-induced graphene. *Sol. Energy Mater. Sol. Cells* **2025**, *282*, 113406.
[31] Li, X. B.; Jiang, L.; Li, X. W.; Qu, L. T.; Zhao, Y.; Wang, J. Q.; Yi, P.; Li, T. Y.; Zhang, X. Y.; Li, J. F. Bifunctional Janus membranes for multicomponent contaminated seawater separation and recovery. *ACS Appl. Mater. Interfaces* **2024**, *16*, 60890–60901.
[32] Li, L.; Gong, P. Y.; Zhang, Y.; Liang, C. C.; Wang, Z. Y.; Wang, P.; Liu, Y. Y.; Cheng, H. F.; Dai, Y.; Zheng, Z. K. et al. Boosting photocatalytic water vapor splitting by nanosecond infrared laser-assisted synthesis of photothermal substrate. *ACS Appl. Energy Mater.* **2025**, *8*, 5190–5198.
[33] Chu, D. K.; Tang, Z. L.; Hu, S. S.; Yang, F. Y.; Qu, S. S.; Mao, W. S.; Yao, P. Aluminum-based solar interfacial evaporator prepared by picosecond laser processing combined with fire treatment used for high-efficiency water-electric cogeneration. *Chem. Eng. J.* **2025**, *515*, 163724.
[34] Zhong, H.; Zhao, Q. H.; Lai, Z. Y.; Xu, D.; Ji, Y. X.; Wang, S. F.; Qin, Q. Efficient and selective lithium extraction from brine water via a photothermal sandwich sieve structure. *Adv. Funct. Mater.* **2025**, *35*, 2418358.
[35] Dang, C. Y.; Nie, H. J.; Cao, X. E.; Cao, Y. T.; Liu, L. J.; Zhu, X. Q.; Zhu, Q. X.; Zhu, L. P.; Xu, G. Y.; Zhu, M. F. System integration for solar-driven interfacial desalination. *Device* **2024**, *2*, 100361.
[36] Zhou, L.; Tan, Y. L.; Wang, J. Y.; Xu, W. C.; Yuan, Y.; Cai, W. S.; Zhu, S. N.; Zhu, J. 3D self-assembly of aluminium nanoparticles for plasmon-enhanced solar desalination. *Nat. Photon.* **2016**, *10*, 393–398.
[37] Luo, S. Q.; Ren, X. H.; Lin, H. W.; Song, H.; Ye, J. H. Plasmonic photothermal catalysis for solar-to-fuel conversion: Current status and prospects. *Chem. Sci.* **2021**, *12*, 5701–5719.
[38] Yang, B.; Li, C. Y.; Wang, Z. F.; Dai, Q. Thermoplasmonics in solar energy conversion: Materials, nanostructured designs, and applications. *Adv. Mater.* **2022**, *34*, 2107351.
[39] Chen, X. D.; Meng, C.; Wang, Y.; Zhao, Q. Q.; Li, Y. J.; Chen, X. M.; Yang, D. W.; Li, Y. X.; Zhou, Y. Laser-synthesized rutile TiO_2 with abundant oxygen vacancies for enhanced solar water evaporation. *ACS Sustainable Chem. Eng.* **2020**, *8*, 1095–1101.
[40] Ali, I.; Zenab Hasan, S.; Garcia, H.; Danquah, M. K.; Imanova, G. Recent advances in graphene-based nano-membranes for desalination. *Chem. Eng. J.* **2024**, *483*, 149108.
[41] Cao, A. Y.; Dickrell, P. L.; Sawyer, W. G.; Ghasemi-Nejhad, M. N.; Ajayan, P. M. Super-compressible foamlike carbon nanotube films. *Science* **2005**, *310*, 1307–1310.
[42] Wan, S. J.; Jiang, L.; Cheng, Q. F. Design principles of high-performance graphene films: Interfaces and alignment. *Matter* **2020**, *3*, 696–707.
[43] Zhang, P. P.; Liu, F.; Liao, Q. H.; Yao, H. Z.; Geng, H. Y.; Cheng, H. H.; Li, C.; Qu, L. T. A microstructured graphene/poly(*N*-isopropylacrylamide) membrane for intelligent solar water evaporation. *Angew. Chem., Int. Ed.* **2018**, *57*, 16343–16347.
[44] Wang, L. R.; Lin, J. G.; Li, Y. Y.; Yang, Y. N.; Liu, X. T.; Wang, Z.; Liu, F.; Sun, X. T.; Yang, T.; Chen, N. et al. Interfacial charge transfer weakens hydrogen bonds between water molecules to accelerate solar water evaporation. *J. Mater. Chem. A* **2023**, *11*, 7662–7669.

[45] Wang, B.; Zhu, H.; Cheng, H. H.; Qu, L. T. Ultradense network hydrogels for rapid solar vapor generation. *Nano Lett.* **2025**, *25*, 14270–14278.
[46] Hu, G.; Liu, H.; Liu, K.; Wang, H.; Wen, X.; Liu, L.; She, Y.; Feng, L.; Niu, R.; Gong, J. All‐in‐one carbon foam evaporators for efficient co‐generation of freshwater and electricity. *Adv. Funct. Mater.* **2025**, *35*, 2423781.
[47] Zhu, B.; Kou, H.; Liu, Z. X.; Wang, Z. J.; Macharia, D. K.; Zhu, M. F.; Wu, B. H.; Liu, X. G.; Chen, Z. G. Flexible and washable CNT-embedded PAN nonwoven fabrics for solar-enabled evaporation and desalination of seawater. *ACS Appl. Mater. Interfaces* **2019**, *11*, 35005–35014.
[48] Zhou, X. Y.; Zhao, F.; Guo, Y. H.; Rosenberger, B.; Yu, G. H. Architecting highly hydratable polymer networks to tune the water state for solar water purification. *Sci. Adv.* **2019**, *5*, eaaw5484.
[49] Li, W. G.; Li, Z.; Bertelsmann, K.; Fan, D. E. Portable low-pressure solar steaming-collection unisystem with polypyrrole origamis. *Adv. Mater.* **2019**, *31*, 1900720.
[50] Zhao, F.; Zhou, X. Y.; Shi, Y.; Qian, X.; Alexander, M.; Zhao, X. P.; Mendez, S.; Yang, R. G.; Qu, L. T.; Yu, G. H. Highly efficient solar vapour generation via hierarchically nanostructured gels. *Nat. Nanotechnol* **2018**, *13*, 489–495.
[51] Zhu, L. L.; Tian, L.; Jiang, S. Y.; Han, L. H.; Liang, Y. Z.; Li, Q.; Chen, S. Advances in photothermal regulation strategies: From efficient solar heating to daytime passive cooling. *Chem. Soc. Rev.* **2023**, *52*, 7389–7460.
[52] Zhu, K. X.; Liao, Q. H.; Hao, X. Z.; Yao, H. Z.; Bai, J. X.; Guang, T. L.; Lin, T. Y.; Cheng, H. H.; Qu, L. T. Low-grade waste heat enables over 80 $L \cdot m^{-2} \cdot h^{-1}$ interfacial steam generation based on 3D superhydrophilic foam. *Adv. Mater.* **2023**, *35*, 2211932.
[53] Zhang, P. P.; Wang, H. Y.; Xia, Z. Y.; Xing, S. J.; Li, J.; Wang, J.; Guo, L. P.; Guo, Z. Y.; Ji, Z. Y.; Qu, L. T. Hydrogen-bond-repairing solar evaporator with reconstructed large-width channels for durable solarizing seawater. *Nano Lett.* **2024**, *24*, 11615–11623.
[54] Jiang, J. Y.; Zhao, H. R.; Li, S. J.; Jin, B. Q.; Wang, R.; Wei, Y.; Li, H. X.; Dai, Y. Q. Nano-to-macroscale insights into solar evaporation: Bridging fundamental principles to intelligent systems. *ACS Nano* **2025**, *19*, 24564–24591.
[55] Lafuma, A.; Quéré, D. Superhydrophobic states. *Nat. Mater.* **2003**, *2*, 457–460.
[56] Song, J. L.; Gao, M. Q.; Zhao, C. L.; Lu, Y.; Huang, L.; Liu, X.; Carmalt, C. J.; Deng, X.; Parkin, I. P. Large-area fabrication of droplet pancake bouncing surface and control of bouncing state. *ACS Nano* **2017**, *11*, 9259–9267.
[57] Liu, X. L.; Yang, J. Y.; Zou, Q. F.; Hu, Y. Y.; Li, P. K.; Tan, L.; Miljkovic, N.; Yang, R. G. Enhancing liquid-vapor phase-change heat transfer with micro/nano-structured surfaces. *ACS Nano* **2025**, *19*, 9513–9589.
[58] Good, R. J. A thermodynamic derivation of Wenzel's modification of young's equation for contact angles; Together with a theory of hysteresis[1]. *J. Am. Chem. Soc.* **1952**, *74*, 5041–5042.
[59] Wenzel, R. N. Resistance of solid surfaces to wetting by water. *Ind. Eng. Chem.* **1936**, *28*, 988–994.
[60] Cassie, A. B. D.; Baxter, S. Wettability of porous surfaces. *Trans. Faraday Soc.* **1944**, *40*, 546–551.
[61] Zhang, W. L.; Wang, D. H.; Sun, Z. N.; Song, J. N.; Deng, X. Robust superhydrophobicity: Mechanisms and strategies. *Chem. Soc. Rev.* **2021**, *50*, 4031–4061.
[62] Wang, D. H.; Sun, Q. Q.; Hokkanen, M. J.; Zhang, C. L.; Lin, F. Y.; Liu, Q.; Zhu, S. P.; Zhou, T. F.; Chang, Q.; He, B. et al. Design of robust superhydrophobic surfaces. *Nature* **2020**, *582*, 55–59.
[63] Xu, N.; Hu, X. Z.; Xu, W. C.; Li, X. Q.; Zhou, L.; Zhu, S. N.; Zhu, J. Mushrooms as efficient solar steam‐generation devices. *Adv. Mater.* **2017**, *29*, 1606762.
[64] Washburn, E. W. The dynamics of capillary flow. *Phys. Rev.* **1921**, *17*, 273–283.
[65] Rye, R. R.; Mann, J. A.; Yost, F. G. The flow of liquids in surface grooves. *Langmuir* **1996**, *12*, 555–565.
[66] Singh, S. C.; ElKabbash, M.; Li, Z. L.; Li, X. H.; Regmi, B.; Madsen, M.; Jalil, S. A.; Zhan, Z. B.; Zhang, J. H.; Guo, C. L. Solar-trackable super-wicking black metal panel for photothermal water sanitation. *Nat. Sustain.* **2020**, *3*, 938–946.
[67] Liang, H. X.; Liao, Q. H.; Chen, N.; Liang, Y.; Lv, G. Q.; Zhang, P. P.; Lu, B.; Qu, L. T. Thermal efficiency of solar steam generation approaching 100% through capillary water transport. *Angew. Chem., Int. Ed.* **2019**, *58*, 19041–19046.
[68] Stratakis, E.; Bonse, J.; Heitz, J.; Siegel, J.; Tsibidis, G. D.; Skoulas, E.; Papadopoulos, A.; Mimidis, A.; Joel, A. C.; Comanns, P. et al. Laser engineering of biomimetic surfaces. *Mater. Sci. Eng. R Rep.* **2020**, *141*, 100562.
[69] Wang, J. S.; Fang, F. Z.; An, H. J.; Wu, S.; Qi, H. M.; Cai, Y. X.; Guo, G. Y. Laser machining fundamentals: Micro, nano, atomic, and close-to-atomic scales. *Int. J. Extrem. Manuf.* **2023**, *5*, 012005.
[70] Chen, C. H.; Tian, Z.; Luo, X.; Jiang, G. C.; Hu, X. Y.; Wang, L. Z.; Peng, R.; Zhang, H. J.; Zhong, M. L. Cauliflower-like micro-nano structured superhydrophobic surfaces for durable anti-icing and photothermal de-icing. *Chem. Eng. J.* **2022**, *450*, 137936.
[71] Li, W. Z.; Chu, D. K.; Wang, Q. W.; Yin, K.; Zhang, H. H.; Qu, S. S.; Yao, P. A salt pollution self-cleaning al based solar desalination evaporator fabricated using a picosecond laser. *J. Mater. Chem. C* **2023**, *11*, 11234–11242.
[72] Yao, H. Z.; Zhang, P. P.; Yang, C.; Liao, Q. H.; Hao, X. Z.; Huang, Y. X.; Zhang, M.; Wang, X. B.; Lin, T. Y.; Cheng, H. H. et al. Janus-interface engineering boosting solar steam towards high-efficiency water collection. *Energy Environ. Sci.* **2021**, *14*, 5330–5338.
[73] Hao, X. Z.; Yao, H. Z.; Zhang, P. P.; Liao, Q. H.; Zhu, K. X.; Chang, J.; Cheng, H. H.; Yuan, J. Y.; Qu, L. T. Multifunctional solar water harvester with high transport selectivity and fouling rejection capacity. *Nat. Water* **2023**, *1*, 982–991.
[74] Zhang, P. P.; Liao, Q. H.; Yao, H. Z.; Cheng, H. H.; Huang, Y. X.; Yang, C.; Jiang, L.; Qu, L. T. Three-dimensional water evaporation on a macroporous vertically aligned graphene pillar array under one sun. *J. Mater. Chem. A* **2018**, *6*, 15303–15309.
[75] Wu, H. F.; Tang, R. J. X.; Zhang, D. S.; Wang, X. Y.; Wang, C. Y.; Jiang, Z. C.; Li, Z. G.; Chen, M. W.; Liu, P. Femtosecond laser opening hierarchical lamination: Micro-nano hybrid scissoring of three-dimensional nitrogen-doped graphene for solar steam generation. *Nano Lett.* **2025**, *25*, 4143–4153.
[76] Jiang, G. C.; Wang, L. Z.; Tian, Z.; Chen, C. H.; Hu, X. Y.; Peng, R.; Li, D. Z.; Zhang, H. J.; Fan, P. X.; Zhong, M. L. Boosting water evaporation via continuous formation of a 3D thin film through triple-level super-wicking routes. *Mater. Horiz.* **2023**, *10*, 3523–3535.
[77] Wang, X. X.; Wang, C. B.; Wang, F.; Tan, P. X.; Jin, J. J.; Lin, X. L.; Zhang, W. H.; Zhao, Z. X.; Wang, L. Aluminum-based Janus evaporator with decoupling photothermal-evaporation interfaces for enduring vapor generation. *Chem. Eng. J.* **2025**, *520*, 165802.
[78] Ye, R. Q.; James, D. K.; Tour, J. M. Laser-induced graphene: From discovery to translation. *Adv. Mater.* **2019**, *31*, 1803621.
[79] Yang, J.; Yu, J. J.; Zhang, K.; Qiao, F.; Yu, G. Laser-induced graphene toward flexible energy harvesting and storage electronics. *Adv. Mater. Technol.* **2024**, *9*, 2301602.
[80] Wang, W. T.; Lu, L. S.; Lu, X. Y.; Liang, Z. B.; Lin, H. H.; Li, Z. H.; Wu, X. H.; Lin, L. H.; Xie, Y. X. Scorpion-inspired dual-bionic, microcrack-assisted wrinkle based laser induced graphene-silver strain sensor with high sensitivity and broad working range for wireless health monitoring system. *Nano Res.* **2023**, *16*, 1228–1241.
[81] Zhu, J. B.; Huang, X.; Song, W. X. Physical and chemical sensors on the basis of laser-induced graphene: Mechanisms, applications, and perspectives. *ACS Nano* **2021**, *15*, 18708–18741.
[82] Chrispin Laila, A.; Singh, S. P. Dual-sided superhydrophobic laser-induced graphene evaporator for efficient desalination and brine treatment under high salinity. *ACS Appl. Mater. Interfaces* **2025**, *17*, 4972–4983.

[83] Misra, U.; Dixit, N.; Singh, S. P. Effect of laser parameters on laser-induced graphene filter fabrication and its performance for desalination and water purification. *ACS Appl. Mater. Interfaces* **2023**, *15*, 7899–7910.

[84] Kothuru, A.; Goel, S. Laser induced graphene on phenolic resin and alcohol composite sheet for flexible electronics applications. *Flex. Print. Electron.* **2020**, *5*, 042001.

[85] Zhang, Z. C.; Song, M. M.; Hao, J. X.; Wu, K. B.; Li, C. Y.; Hu, C. G. Visible light laser-induced graphene from phenolic resin: A new approach for directly writing graphene-based electrochemical devices on various substrates. *Carbon* **2018**, *127*, 287–296.

[86] Fan, J.; Wang, Z.; Wu, Y. J.; Liao, G. L.; Shi, T. L.; Xiong, F.; Long, H. Laser-induced graphene derived from aramid nanofiber films as flexible strain sensors. *ACS Appl. Nano Mater.* **2025**, *8*, 21451–21461.

[87] Nasser, J.; Groo, L.; Zhang, L. S.; Sodano, H. Laser induced graphene fibers for multifunctional aramid fiber reinforced composite. *Carbon* **2020**, *158*, 146–156.

[88] Yang, Z. H.; Wang, B.; Peng, Y. B.; Yuan, Y.; Tang, Z. Q.; Meng, W.; Zhao, Y. H.; Wang, X. L. One-step sustainable preparation of laser induced S-doped graphene for assembly of high-performance supercapacitors. *J. Clean. Prod.* **2024**, *450*, 141956.

[89] Yang, Z. H.; Yuan, Y.; Wang, B.; Shen, X. J.; Wang, X. L.; Yuan, T. Q. A solely biobased strain sensor with an ultra-precision response via a surface graphitization strategy. *J. Mater. Chem. A* **2023**, *11*, 24928–24938.

[90] Bressi, A. C.; Amaro, L. P.; Pizzo, B.; Marino, A.; Ciofani, G.; Greco, F. Laser-induced graphene from wood-based composites: Integrating circuits in bioderived furniture. *Adv. Sustain. Syst.* **2025**, *9*, e00565.

[91] Dreimol, C. H.; Guo, H. Z.; Ritter, M.; Keplinger, T.; Ding, Y.; Günther, R.; Poloni, E.; Burgert, I.; Panzarasa, G. Sustainable wood electronics by iron-catalyzed laser-induced graphitization for large-scale applications. *Nat. Commun.* **2022**, *13*, 3680.

[92] Sun, W. Q.; Xiang, L.; Luo, Z. B.; Wang, H.; Li, D.; Pan, A. L. Cost-effective fabrication of liquid metals via a laser induced graphene stamp for highly-stretchable integrated optoelectronics. *Nano Res.* **2024**, *17*, 7603–7613.

[93] Chen, Z. C.; Li, Q.; Chen, X. M. Porous graphene/polyimide membrane with a three-dimensional architecture for rapid and efficient solar desalination via interfacial evaporation. *ACS Sustainable Chem. Eng.* **2020**, *8*, 13850–13858.

[94] Han, D. D.; Chen, Z. D.; Li, J. C.; Mao, J. W.; Jiao, Z. Z.; Wang, W.; Zhang, W.; Zhang, Y. L.; Sun, H. B. Airflow enhanced solar evaporation based on Janus graphene membranes with stable interfacial floatability. *ACS Appl. Mater. Interfaces* **2020**, *12*, 25435–25443.

[95] Peng, Y. Y.; Zhao, W. W.; Ni, F.; Yu, W. J.; Liu, X. Q. Forest-like laser-induced graphene film with ultrahigh solar energy utilization efficiency. *ACS Nano* **2021**, *15*, 19490–19502.

[96] Huang, L. B.; Ling, L.; Su, J. J.; Song, Y.; Wang, Z. Y.; Tang, B. Z.; Westerhoff, P.; Ye, R. Q. Laser-engineered graphene on wood enables efficient antibacterial, anti-salt-fouling, and lipophilic-matter-rejection solar evaporation. *ACS Appl. Mater. Interfaces* **2020**, *12*, 51864–51872.

[97] Xu, R.; Luo, P. G.; Zhao, H. Y.; Lu, H.; Zhou, T. *In-situ* laser-induced biomimetic 3D-arched graphene with grass-like structures for efficient seawater desalination. *J. Mater. Chem. A* **2025**, *13*, 12611–12624.

[98] Dong, X. R.; Shao, J.; Huang, L. H.; Zhu, X. D.; Luo, H.; Zhou, X. F.; Liu, W. L.; Song, Y. X. Photothermal composite coating-enhanced laser-induced graphene evaporator for efficient seawater desalination. *Chem. Eng. J.* **2025**, *519*, 165619.

[99] Ko, Y.; Lee, S.; Jang, J.; Kwon, G.; Lee, K.; Jeon, Y.; Lee, A.; Park, T.; Kim, J.; You, J. Nanocellulose-based interfacial solar evaporator: Integrating sustainable materials and micro-/nano-architectures for solar desalination. *Adv. Funct. Mater.* **2025**, *35*, 2414576.

[100] Cheng, J. F.; Fan, X. X.; Wan, L.; Wang, Z. L.; Tang, S. Q.; Wu, D.; Wang, D.; Liu, C. L.; Cao, Z. Laser-induced carbonization strategy for designing efficient dual-layer solar wastewater evaporator. *Chem. Eng. J.* **2024**, *495*, 153498.

[101] Zhang, P. P.; Li, J.; Xing, S. J.; Jia, Q.; Wang, J.; Bi, J. T.; Guo, Z. Y.; Wang, L.; Ji, Z. Y.; Qu, L. T. Solar evaporators for saline water: Sustainable clean water harvesting and critical mineral resources extraction. *ACS Nano* **2025**, *19*, 11625–11647.

[102] Liu, Y. H.; Zhang, Z. W.; Wang, J. G.; Hu, C.; Tang, J. X.; Shi, M.; Cui, H. Y.; Qi, D. F. Janus-structured lignin hydrogel evaporator via laser direct writing for high efficiency seawater desalination and solar power generation. *Chem. Eng. J.* **2025**, *513*, 162853.

[103] Fang, S. M.; Lu, H.; Chu, W. C.; Guo, W. L. Mechanism of water-evaporation-induced electricity beyond streaming potential. *Nano Res. Energy* **2024**, *3*, e9120108.

[104] Wei, Y. J.; Zhang, J.; Huang, Z. J.; Yu, Q. X.; Liang, G. W.; Rao, L. S.; Chao, X. J.; Li, J. L.; Wu, J. N.; Yu, S. D. Laser-scribed wood photoabsorbers for sustainable interfacial solar steam and electricity co-generation. *Energy Convers. Manage.* **2025**, *344*, 120291.

[105] Guo, S. H.; Li, X. H.; Li, J.; Wei, B. Q. Boosting photocatalytic hydrogen production from water by photothermally induced biphase systems. *Nat. Commun.* **2021**, *12*, 1343.

[106] Xue, C. R.; Zhang, Q.; Shen, Y.; Hu, S. L.; Chang, Q.; Wang, H. Q.; Li, N.; Yang, J. L. Laser thermal synthesis of reduced graphene oxide/CuS nanocomposites for efficient solar-driven water purification. *Sep. Purif. Technol.* **2022**, *294*, 121168.

[107] Hsiao, Y. S.; Lin, C. Y.; Weng, L. Y.; Hsu, C. H.; Cheng, T. H.; Huang, J. H.; Wu, N. J.; Pang, W. K.; Hsu, S. C.; Weng, H. C. et al. *In-situ* synthesis of NbC nanoparticle-decorated polyimide-derived graphene for enhanced thermal management. *Chem. Eng. J.* **2024**, *483*, 149007.

[108] Wei, Y. J.; Li, W. H.; Zhang, S. C.; Yu, J. D.; Tang, Y.; Wu, J. N.; Yu, S. D. Laser-induced porous graphene/CuO composite for efficient interfacial solar steam generation. *Adv. Funct. Mater.* **2024**, *34*, 2401149.

[109] Huang, Z. J.; Wei, Y. J.; Zhang, J.; Chen, P. H.; Zeng, H. Z.; Chen, S. H.; Rao, L. S.; Wu, J. N.; Yu, S. D. Laser-induced graphene on gelatin-functionalized cellulose paper for efficient interfacial solar steam generation. *Small* **2025**, *21*, e05931.

[110] Zhang, J.; Wei, Y. J.; Chen, P. H.; Huang, Z. J.; Yu, Q. X.; Tan, J.; Zeng, H. Z.; Yu, S. D. Iron-catalyzed laser-induced graphene on cellulose paper for solar-driven interfacial evaporation. *Mater. Horiz.* **2025**, *12*, 7346–7357.

[111] Fojtik, A.; Giersig, M.; Henglein, A. Formation of nanometer-size silicon particles in a laser induced plasma in SiH_4. *Ber. Bunsenges. Phys. Chem.* **1993**, *97*, 1493–1496.

[112] Forsythe, R. C.; Cox, C. P.; Wilsey, M. K.; Müller, A. M. Pulsed laser in liquids made nanomaterials for catalysis. *Chem. Rev.* **2021**, *121*, 7568–7637.

[113] Kanitz, A.; Kalus, M. R.; Gurevich, E. L.; Ostendorf, A.; Barcikowski, S.; Amans, D. Review on experimental and theoretical investigations of the early stage, femtoseconds to microseconds processes during laser ablation in liquid-phase for the synthesis of colloidal nanoparticles. *Plasma Sources Sci. Technol.* **2019**, *28*, 103001.

[114] Manshina, A. A.; Tumkin, I. I.; Khairullina, E. M.; Mizoshiri, M.; Ostendorf, A.; Kulinich, S. A.; Makarov, S.; Kuchmizhak, A. A.; Gurevich, E. L. The second laser revolution in chemistry: Emerging laser technologies for precise fabrication of multifunctional nanomaterials and nanostructures. *Adv. Funct. Mater.* **2024**, *34*, 2405457.

[115] Sylvestre, J. P.; Poulin, S.; Kabashin, A. V.; Sacher, E.; Meunier, M.; Luong, J. H. T. Surface chemistry of gold nanoparticles produced by laser ablation in aqueous media. *J. Phys. Chem. B* **2004**, *108*, 16864–16869.

[116] Amendola, V.; Meneghetti, M. Laser ablation synthesis in solution and size manipulation of noble metal nanoparticles. *Phys. Chem.*

Chem. Phys. **2009**, *11*, 3805–3821.
[117] Spellauge, M.; Tack, M.; Streubel, R.; Miertz, M.; Exner, K. S.; Reichenberger, S.; Barcikowski, S.; Huber, H. P.; Ziefuss, A. R. Photomechanical laser fragmentation of IrO_2 microparticles for the synthesis of active and redox-sensitive colloidal nanoclusters. *Small* **2023**, *19*, 2206485.
[118] Sajti, C. L.; Sattari, R.; Chichkov, B. N.; Barcikowski, S. Gram scale synthesis of pure ceramic nanoparticles by laser ablation in liquid. *J. Phys. Chem. C* **2010**, *114*, 2421–2427.
[119] Tselikov, G. I.; Ermolaev, G. A.; Popov, A. A.; Tikhonowski, G. V.; Panova, D. A.; Taradin, A. S.; Vyshnevyy, A. A.; Syuy, A. V.; Klimentov, S. M.; Novikov, S. M. et al. Transition metal dichalcogenide nanospheres for high-refractive-index nanophotonics and biomedical theranostics. *Proc. Natl. Acad. Sci. USA* **2022**, *119*, e2208830119.
[120] Chernikov, A. S.; Tselikov, G. I.; Gubin, M. Y.; Shesterikov, A. V.; Khorkov, K. S.; Syuy, A. V.; Ermolaev, G. A.; Kazantsev, I. S.; Romanov, R. I.; Markeev, A. M. et al. Tunable optical properties of transition metal dichalcogenide nanoparticles synthesized by femtosecond laser ablation and fragmentation. *J. Mater. Chem. C* **2023**, *11*, 3493–3503.
[121] Johny, J.; Li, Y.; Kamp, M.; Prymak, O.; Liang, S. X.; Krekeler, T.; Ritter, M.; Kienle, L.; Rehbock, C.; Barcikowski, S. et al. Laser-generated high entropy metallic glass nanoparticles as bifunctional electrocatalysts. *Nano Res.* **2022**, *15*, 4807–4819.
[122] Gurbatov, S. O.; Modin, E.; Puzikov, V.; Tonkaev, P.; Storozhenko, D.; Sergeev, A.; Mintcheva, N.; Yamaguchi, S.; Tarasenka, N. N.; Chuvilin, A. et al. Black Au-decorated TiO_2 produced via laser ablation in liquid. *ACS Appl. Mater. Interfaces* **2021**, *13*, 6522–6531.
[123] Singh, S. C.; Banjarnahor, D.; Tang, L. H.; Wang, H. B.; Wei, R.; Guo, C. L. Real-life solar-thermal water purification exceeding 300% efficiency using 2D planar interfacial evaporator. *Adv. Funct. Mater.* **2025**, *35*, 2501538.
[124] Tang, Z. L.; Hu, S. S.; Chu, D. K.; Qu, S. S.; Yang, Y. Y.; Yao, P. Aluminum-based solar seawater desalination interface evaporator processed by picosecond laser combined with fire treatment. *Desalination* **2025**, *593*, 118239.
[125] Yin, K.; Yang, S.; Wu, J. R.; Li, Y. J.; Chu, D. K.; He, J.; Duan, J. A. Femtosecond laser induced robust Ti foam based evaporator for efficient solar desalination. *J. Mater. Chem. A* **2019**, *7*, 8361–8367.
[126] Tang, Z. L.; Hu, S. S.; Chu, D. K.; Liu, W. B.; Qu, S. S.; Yao, P. Micronano structured polyimide films fabricated using a femtosecond laser for seawater desalination. *ACS Appl. Nano Mater.* **2025**, *8*, 17977–17985.
[127] Luo, Y. T.; Chen, Z. C.; Li, Q.; Chen, X. M. Laser-induced porous graphene on a polyimide membrane with a melamine sponge framework (PI@MS) for long-term stable steam generation. *ACS Appl. Energy Mater.* **2021**, *4*, 9766–9774.
[128] Zhu, S. H.; Lei, Z. W.; Dou, Y. J.; Lou, C. W.; Lin, J. H.; Li, J. W. Sputter-deposited nickel nanoparticles on Kevlar fabrics with laser-induced graphene for efficient solar evaporation. *Chem. Eng. J.* **2023**, *452*, 139403.
[129] Wang, Y. L.; Li, G. J.; Chan, K. C. Cost-effective and eco-friendly laser-processed cotton paper for high-performance solar evaporation. *Sol. Energy Mater. Sol. Cells* **2020**, *218*, 110693.
[130] Li, H. R.; Fan, R. C.; Zhang, F. D.; Cui, Z. W.; Wu, T. T.; Huang, Q.; Kang, F. Y.; Cai, Y. H.; Zhang, Q. C.; Tian, D. Engineering wood-MOF networks to realize multilevel weak water interactions for highly-efficient solar water-power cogeneration. *Chem. Eng. J.* **2025**, *509*, 161332.
[131] Liu, F. H.; Lou, D. Y.; Liang, E. K.; Gu, Y. J.; Wang, Z.; Shi, X. W.; Bradley, R.; Zhao, B. Y.; Wu, W. P. Nanosecond laser patterned porous graphene from monolithic mesoporous carbon for high-performance solar thermal interfacial evaporation. *Adv. Mater. Technol.* **2021**, *6*, 2101052.
[132] Ma, C. R.; Yan, J. H.; Huang, Y. C.; Wang, C. X.; Yang, G. W. The optical duality of tellurium nanoparticles for broadband solar energy harvesting and efficient photothermal conversion. *Sci. Adv.* **2018**, *4*, eaas9894.

This is an open access article under the terms of the Creative Commons Attribution 4.0 International License (CC BY 4.0, https://creativecommons.org/licenses/by/4.0/).

© The Author(s) 2026. Published by Tsinghua University Press.